

Stefan Hofmann, BSc

**Noise, Vibration, and Harshness -
Characteristics of Sub-Fractional Horsepower
Fan Drives**

Master's Thesis

Submitted in Partial Fulfillment of the Requirements for the Degree of

**Diplom-Ingenieur
(Dipl.-Ing.)**

in

Electrical Engineering

at

Graz University of Technology

In Cooperation with

Christian Doppler Laboratory for Brushless Drives
for Pump and Fan Applications, Graz, Austria

and

Mechatronic Systems GmbH, Wies, Austria

Supervisor: Univ.-Prof. Dr.-Ing. Annette Mütze

Co-Supervisor: Dipl.-Ing. Stefan Leitner

Electric Drives and Machines Institute

Graz University of Technology

2019

AFFIDAVIT

I declare that I have authored this thesis independently, that I have not used other than the declared sources/resources, and that I have explicitly indicated all material which has been quoted either literally or by content from the sources used. The text document uploaded to TUGRAZonline is identical to the present master's thesis.

Date

Signature

Contents

Abstract	V
Zusammenfassung	VII
Aim and scope	IX
Acknowledgement	XI
1 Introduction	1
1.1 Context	1
1.2 Evaluation of automotive auxiliary drives	3
1.3 Drive types under investigation	8
1.4 Characteristics of small electric drives	15
1.5 Subjective sound sensibility	16
1.6 Air-borne sound measurements	17
1.7 Structure-borne sound measurements	18
1.8 Noise assessment	18
2 Fan drives	21
2.1 Introduction	21
2.2 Fan type overview	21
2.3 Axial fans	25
2.4 Radial fans	26
2.5 Comparison	26
3 Sources of noise and vibrations in electrical machines	29
3.1 Introduction	29
3.2 Mechanical sources	31
3.3 Electromagnetic sources	32
3.4 Aerodynamic sources	34

3.5	Excitation frequencies	37
3.5.1	Mechanical excitation frequencies	38
3.5.2	Aerodynamic excitation frequencies	40
3.5.3	Electromagnetic excitation frequencies	41
3.6	Common causes of noise and vibrations in electrical machines	42
4	Preliminary investigations	43
4.1	Experimental setup: air-borne sound measurement	43
4.2	Experimental setup: structure-borne sound and current measurements	45
4.3	Tested fan systems	46
4.4	Stator excitation investigations	47
4.5	Current measurements	49
4.6	Comparison: measured versus approximated current waveforms	52
4.7	Influence of rotor imbalance	54
4.8	Investigations of blade passing noise (BPN)	55
4.9	Comparison: acceleration, current, and microphone measurements	56
5	Measurements in a low reflection chamber	59
5.1	Experimental setup: air-borne sound measurements	60
5.1.1	Hemispherical measurement setup	60
5.1.2	In- and outflow noise separation measurement setup	62
5.2	Experimental setup: structure-borne sound measurements	62
5.2.1	Acceleration sensor measurement setup	63
5.2.2	Force sensor measurement setup	64
5.3	Experimental setup: standardized measurements	65
5.4	Fan systems under investigation	66
5.5	Data processing and signal conditioning	66
5.5.1	Accelerometer measurements	67
5.5.2	Microphone measurements	69
5.6	Measurement results	73
5.6.1	Noise position dependence	74
5.6.2	Noise speed dependence	75
5.6.3	Separation of in- and outflow noise	77
5.6.4	Standardized measurements	78
6	Conclusions and future work	83

6.1	Conclusions	83
6.2	Future work	84
	Bibliography	87
	List of figures	93
	List of tables	97

Abstract

The demand for low-noise auxiliary drives has been increasing in the automotive industry, as the entire noise level in the vehicle interior is continuously decreasing. Simultaneously, the number of auxiliary drives is increasing, because of the need of safety, performance, and comfort equipment. Especially in electric vehicles, the application of conventional auxiliary drives, the noise of which is than masked by that of the combustion engine, may not be possible.

Another challenge is the lack of noise standards the auxiliary drives have to comply with. Developing auxiliary drives, the focus used to be primarily on cost, rather than noise behavior. As a result, the noise standards are still at an early stage of development. Hence, there is a need to study the *Noise, Vibration, and Harshness (NVH)* behavior of these drives, to which the following work is intended to contribute. The main focus is on noise generation and emission of electric auxiliary drives (fan drives in particular), whose *NVH* characteristics are studied extensively.

In the theoretical part, a literature review is presented determining the current state-of-the-art. The number of auxiliary drives, the motor types, and their application in middle-class-vehicles are discussed in more detail. Furthermore, the sources as well as the causes of noise generation and emission are discussed, and the fundamentals of psychoacoustics and acoustic measurement technology are described. In order to emphasize the importance of fan motors in this context, a comprehensive overview of common fan types as well as their application areas is given and their characteristics are explained.

The practical part of this thesis consists of measurements and analyses of the air-borne sound, structure-borne sound, and the current. In a first stage, the measurements have been performed using readily available equipment. Later on, more sophisticated measurements have been carried out in an anechoic chamber to analyze several fans in detail. Finally, the results are compared and evaluated based on one-third octave band analyses. This work ends with a conclusion of the main results and an outlook.

Zusammenfassung

In der Automobilindustrie steigt stetig die Nachfrage nach immer leiser werdenden Hilfsantrieben, da der Geräuschpegel im Fahrzeuginnenraum sinkt und deren emittierte Geräusche von den Fahrzeuginsassen oft als unangenehm wahrgenommen werden. Gleichzeitig steigt aber die Anzahl der Hilfsantriebe in Fahrzeugen aufgrund des steigenden Bedarfs an Sicherheits-, Performance-, und Comfort-Equipment. Eine besondere Anforderung stellen dabei Elektrofahrzeuge dar, da deren Antrieb bei weitem nicht den Geräuschpegel eines Verbrennungsmotors aufweist. Somit weisen diese eine geringe Lärmbelastung im Innenraum auf, was zu einer vermehrten Wahrnehmung der emittierten Geräusche der Hilfsantriebe führt.

Eine weitere Herausforderung ist die Tatsache, dass bis vor wenigen Jahren lediglich der Preis, nicht aber die Geräuscheigenschaften dieser Hilfsantriebe im Vordergrund der Forschung standen und somit entsprechende Normen erst in der Entwicklung sind. Dadurch wird die Beschäftigung mit dem Thema *Noise, Vibration, and Harshness (NVH)* dringend notwendig, wozu die folgende Arbeit einen Beitrag leisten soll.

Diese Arbeit beschäftigt sich folglich mit der Geräuschentwicklung von elektrischen Hilfsantrieben und geht im Speziellen auf jene von Lüftern ein. Dabei wird der Frage nachgegangen, welche *NVH*-Charakteristiken elektrische Hilfsantriebe aufweisen.

Im theoretischen Teil wird eine Literaturrecherche durchgeführt, um eine Basis für die Thematik zu schaffen und den Stand der Technik zu ermitteln. Dabei wird auf die Anzahl an Hilfsantrieben, die verwendeten Motortypen und deren Verwendung in Mittelklassefahrzeugen genauer eingegangen.

Außerdem werden die Ursachen der Geräuschentwicklung thematisiert und die Grundlagen der Psychoakustik und der akustischen Messtechnik beschrieben. Um die Wichtigkeit der Lüfterantriebe in diesem Zusammenhang zu unterstreichen, wird ein umfangreicher Überblick der gängigen Lüfter-Typen sowie deren Anwendungsbereiche und Eigenschaften gegeben.

Im praktischen Teil dieser Arbeit werden Messungen des Luftschalls, Körper-

schalls und Stroms durchgeführt, ausgewertet und analysiert. Dabei werden diese Messungen in einer ersten Phase mit einfacher Technik gemessen, im späteren Verlauf in einem reflexionsarmen Raum mit sehr präzisen Messgeräten und diversen Lüftern durchgeführt. Abschließend sollen die Ergebnisse anhand von Terzbandanalysen miteinander verglichen und ausgewertet werden. Den Abschluss dieser Arbeit bildet ein Resümee, das die Ergebnisse nochmals zusammenfasst und diskutiert und einen Ausblick auf zukünftige Entwicklungen geben soll.

Aims and scope

The demand for low-noise auxiliary drives in the automotive industry has increased as of late, because cars are becoming more and more quiet. The overall aim is to influence the noise development in the vehicle interior through specific optimization of the auxiliary drive. For this, however, many characteristics still have to be studied, whereby this thesis should form a foundation having the following targets.

First of all, a literature review should be carried out to determine the state-of-the-art, the number and types of auxiliary drives in the automotive sector, as well as proper measurement methods for NVH characterization. The main focus of this work should be on sub-fractional horsepower fan drives. To separate the noise sources, an essential task is to detect the frequency components. These can be measured as airborne sound microphones, and structure-borne sound using acceleration or force sensors. In addition, the supply current should be measured and evaluated too. Experiments are to be carried out in which on the one hand the aerodynamic noise is greatly reduced (for example by removing the fan blades), and on the other hand the frequency range of the turbulent in- and outflow noise is to be separated. In addition, a list of calculations of the typical frequencies occurring due to the motor characteristics or possible defects shall be compiled and validated. Since the emitted noise has a directional and speed dependency, it should be investigated as a function of distance, speed, and position. Therefore, the measured values of the sound pressure level (SPL) at various positions for different distances and speeds should be compared with available analytical estimation methods. Finally, measurement according to a selected industrial standard should be performed and evaluated.

Acknowledgment

This thesis was written within the framework of the Christian Doppler Laboratory for Brushless Drives for Pump and Fan Applications at Graz University of Technology, Austria. The financial support of the Christian Doppler Association (CDG) is gratefully acknowledged.

The successful completion of this thesis was made possible through the contribution of a number of people. I would like to express my profound gratitude to the Electric Drives and Machines Institute at Graz University of Technology, in particular my supervisor Prof. Annette Mütze for her support. I also want to thank my co-supervisor DI Stefan Leitner for his motivation and assistance throughout the whole project.

My sincere thanks also go to the Electronic Music and Acoustic Institute at the University of Music and Performing Arts, Austria. In this regard, I would like to thank Ass. Prof. Franz Zotter, Dr. Mathias Frank, and DI Stefan Warum for the opportunity to perform the measurements, the provided resources, as well as the excellent assistance.

I would also like to thank the Mechatronic Systems GmbH for the good cooperation, especially DI Hans-Jörg Gasser, Dr. Markus Mosshammer, and Ing. Christopher Stopper.

Chapter 1

Introduction

1.1 Context

The demand for overall noise level reduction in cars has increased recently. At the same time, the number of auxiliary drives in cars has also increased significantly, for reasons of comfort, safety, and performance. Especially in electric vehicles, the application of conventional auxiliary drives, the noise of which is then masked by that of the combustion engine or other dominant noise sources, may not be possible [1, p. 394], [2, p. 1]. Figure 1.1 shows a schematic overview of the in-car noise development over the last decades. As can be seen, the noise of auxiliary drives may reappear and become disturbing. Hence, it is of utmost importance to have profound knowledge of the noise, vibration, and harshness (NVH) behavior of these drives. The aim of this thesis is to determine the NVH characteristics of sub-fractional horsepower fan drives, which will help optimize auxiliary drives with respect to their noise emissions.

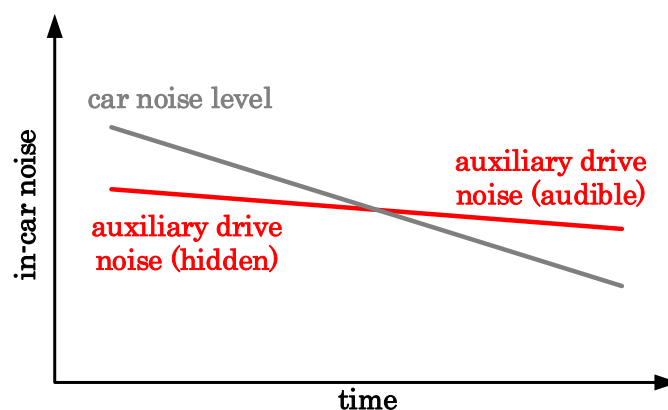


Figure 1.1: Schematic in-car noise development [1, p. 394].

According to the German electrical and electronic manufacturers' association (ZVEI), the production volume for the whole electric drive technology in 2017 was about 8.9 billion Euro. The percentage distribution of the different areas involved are illustrated in Figure 1.2 [3, p. 3]. Small electric drives hold a 21.7 percentage stake, which stresses the importance and the potential impact of advances in the auxiliary drive sector.

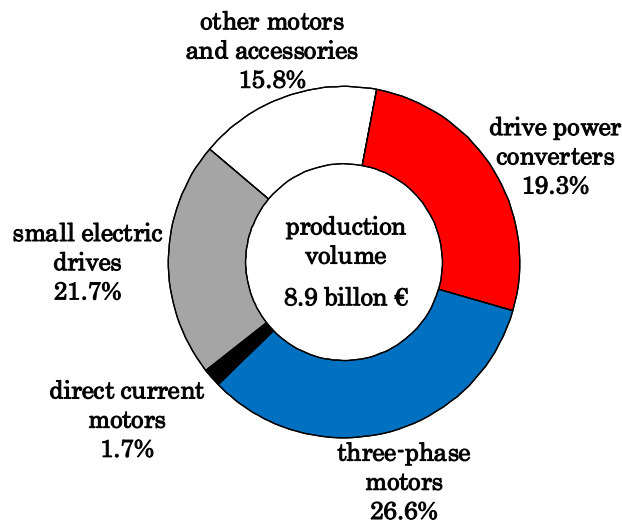


Figure 1.2: Percentage distribution of the production volume of electric drives in 2017 [3, p. 3].

As opposed to integral horsepower electric motors and drives, fractional horsepower drives (which can be found, e.g., in household appliances and vehicles) are exempted from standardization. In fact, these small electric drives are customized for each application. The acoustic behavior of small electric drives is a complex topic [4, p. 12], [5, p. 372], [6, p. 374]. For a long time, noise standard for automotive auxiliary drives did not exist and their noise requirements were inaccurately described. Recently, as the noise of small electric drives has become more relevant, the automotive sector initiated the development of such standards.

The riding pleasure in a car is not only affected by noise (audible perception of oscillations) but also by vibrations (tactile perception of oscillations). Whether either of them is perceived as disturbing strongly depends on the frequency.

Hence, the well known acronym **NVH** (Noise, Vibration, and Harshness) has been introduced which is understood to describe oscillation phenomena, based on the following three frequency ranges [7, p. 163 - 165].

- **Vibrations:** 0-20 Hz
- **Harshness:** 20-50 Hz
- **Noise:** 50-20000 Hz

Vibrations are defined as oscillations up to 20 Hz, which are perceived exclusively as vibrations of the structure (road-excited vibrations being an example). The **Harshness** represents a transition zone, which is caused by oscillations in the range from 20 to 50 Hz. This type of oscillation is both audible and tactile. A typical example is the idle shaking of a combustion engine. **Noise** describes audible oscillations in the range up to 20 kHz. In automotive acoustics, these oscillations are rather located in the area of comfort than in driving dynamics. All in all, psychoacoustics describes the effect of a physical sound event on a human, see Chapter 1.5.

1.2 Evaluation of automotive auxiliary drives

Over the last decades, a majority of cars were powered by combustion engines. However, due to political and environmental reasons, there might be a paradigm shift from cars with combustion engines to electric cars, hybrid cars being a temporary solution. The UK and France already set dates to ban combustion engines, other countries are likely to follow. Besides the main drive in electric cars and alternators in conventional cars, there are many more electric drives which are not recognized at the first glance [8]. In fact, a lot of **auxiliary drives enhance the performance, safety, and comfort**. Even though the **total number of auxiliary drives** in a car strongly depends on the vehicle's equipment (and hence price range), it amounts to **about 100 for a mid-size executive car** (e.g., Audi A6). Figure 1.3 shows an overview of the usage of auxiliary electric drives in a car.

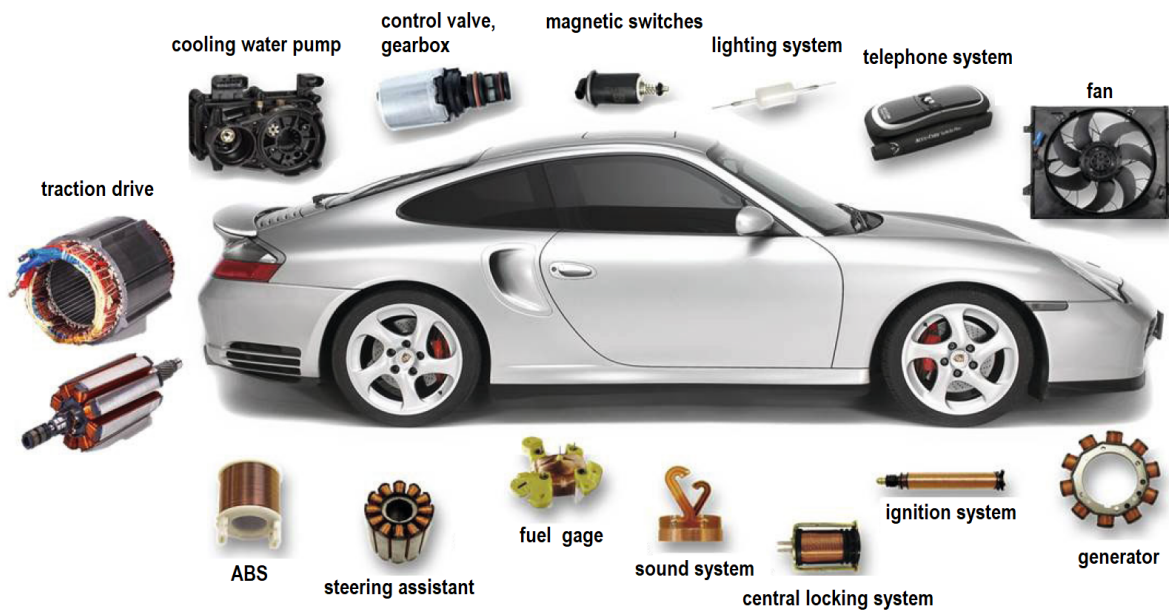


Figure 1.3: Overview of the usage of small electric drives in a car [9, p. 81].

These auxiliary drives can be divided into three main categories:

- **performance**-related drives
- **safety**-related drives
- **comfort**-related drives

The **performance**-related drives are directly linked to the engine or power train (e.g., engine cooling pump, oil pump, alternator). The **safety**-related drives are directly or indirectly linked to the drivability and handling of the car (e.g., windshield wiper, headlamp beam height control, screen wash liquid pump). The **comfort**-related drives are not necessary for the functioning of the car, but they increase both the driver and passenger comfort. Based on this classification, Figure 1.4 shows the percentage distribution of said categories for a mid-size executive car [10, p. 5 - 7].

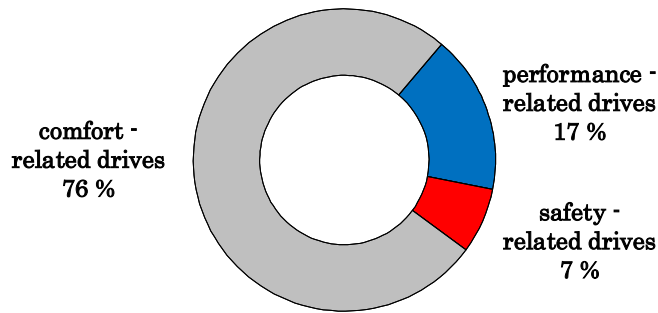


Figure 1.4: Percentage distribution of small electric drives in a mid-size executive car [10, p. 7].

According to Figure 1.4, the largest number of auxiliary drives is used in comfort equipment. Yet, it has to be taken into account, that the number of comfort-related electric drives used in a car is highly dependent on the chosen equipment. In 2013, Mercedes Benz published the number of comfort-related electric drives in their S-Class, see Table 1.1 .

function	quantity
ventilation, air conditioning system	21
seat actuator	54
steering wheel adjustment	2
magnetic valves for massage seat (two seats)	28
window lifter	4
exterior mirror	5
door and tailgate closer	5
sound system (tweeter adjustment)	2
steering wheel vibrator	1
fan, main display	1
sunroof and window shade	5
seat belt bringer and stretcher	4
DVD - deck	2
	Σ 132

Table 1.1: Number of auxiliary drives to increase the comfort of the Mercedes S-Class in 2013 [11].

In general, auxiliary drives are customized, designed for a specific task, meeting various application-specific requirements. Hence, they are highly integrated, posing a mechatronic system. The **choice of motor type** strongly depends on the drive's duty cycle. The following two main application types are distinguished:

- **Short-term** applications
- **Long-term** applications

Traditional **brushed DC (BDC) motors** and **stepper motors** are mainly used in **short-term** applications (e.g., window lifter, seat actuator, mirror adjustment). The main reasons for using **BDC motors** are their low price and simplicity of control. In **long-term** applications (e.g., windscreen wiper, ventilation, or pumps), **brushless direct current (BLDC)** and **brushless alternating current (BLAC) motors** have considerable advantages over **BDC motors** such as high power density and efficiency as well as low maintenance [8]. Table 1.2 shows automotive auxiliary drives and the used motor types. A general trend towards the usage of **BLDC and BLAC motors** in more and more applications can be identified (in particular, see engine cooling fan and fuel pump in Table 1.2).

application \ motor type	BLDC / BLAC	BDC	stepper
	ESP/ABS motor		X
EVP (electric vacuum pump)		X	
EMB (electric-mechanical breaking)	X		
sunroof motor		X	
closure motor		X	
window lift motor		X	
seat adjustment motor		X	
steering column adjuster		X	
engine cooling fan	X	X	
seat ventilation	X		
sensor ventilation	X		
main heat- & AC fan		X	
thermo-management fan	X		
sensor blower	X		
active steering support	X		
wash water pump		X	
cooling water pump	X		
fuel pump	X	X	
oil pump	X		
air throttle valve		X	
windscreen wiper motor		X	
expansion valves			X
mirror adjustment		X	X
headlight range adjustment			X
fuel and speed gage			X

Table 1.2: Automotive applications and their motor types [12–16].

1.3 Drive types under investigation

As presented in Table 1.2, different motor types are deployed in automotive auxiliary drive applications. In this thesis, the focus is on permanent magnet synchronous motors (PMSM), which are primarily driven by voltage-sourced inverters. As opposed to brushed DC motors, where the commutation is mechanically realized, PMSMs are electronically commutated using power electronic switches. Generally, these brushless motors consist of a rotor with permanent magnets and a stator with at least one winding. For decades, the electronic commutation was performed using transistors and diodes. Nowadays, metal-oxide-semiconductor field-effect transistors (MOSFET) can be found in every converter. Operating PMSMs, it is important that the switching process is happening at the right rotor position to maximize the torque. Hall sensors, encoders, and resolvers can be used to detect the rotor position of PMSMs. In addition, sensorless control strategies are available [17, p. 7-9], [18].

Theoretically, they can be implemented with any number of phases, but the single- and three-phase systems are by far the most common ones for reasons of cost-performance tradeoffs, material utilization, as well as manufacturing and operating complexity. Usually, the stator is made of laminated steel to reduce the eddy current losses and the coil are placed in slots. To get a high torque, the remanence flux density of the magnet should be high. There are different kinds of permanent magnets such as ferrite and rare earth alloy magnets (e.g., SmCo, NdFeB) [17, p. 7-9], [18].

Another distinction is made between the position of stator and rotor. There are two main groups, the **outer-rotor** and the **inner-rotor** types. Inner-rotor machines show improved heat dissipation (because the stator and hence the winding is on the outside) and low inertia (since the air-gap radius is relatively small for a given volume). Outer-rotor variants are characterized by high torque but also increased inertia, making them unsuitable for dynamic operation [19, p. 117 - 121]. These motors are often deployed in hard disk drives (as the high inertia leads to a smooth operation) and fan drives (as the blades can be mounted directly onto the rotor, reducing the size of the application) [19, p. 117 - 121]. Outer-rotor machines also have the advantage that they can be wound from the outside, omitting the need of a needle winder, ensuring an easier and fast winding process [9, p. 196 - 204]. In this thesis, the focus is on outer-rotor motors as they are the most common topology found in auxiliary fan drives.

There are two main brushless permanent magnet motor types:

- Brushless direct current (**BLDC**)
- Brushless alternating current (**BLAC**)

As opposed to the operation of BLDC and BLAC motors, their construction is very similar. Hence, they share the same equivalent circuit which is illustrated in Figure 1.5 for a single-phase. The resistance R represents the copper losses and the phase inductance L can be modeled as a leakage inductance L_σ and a main inductance L_m . The back-EMF u_{EMF} can be modeled as a voltage source, the shape of which depends on the magnetization pattern of the permanent magnet. The phase voltage u_p supplied to the motor by the inverter is usually pulse-width modulated. The phase current i_p depends on the magnitude and phase of u_p and u_{EMF} .

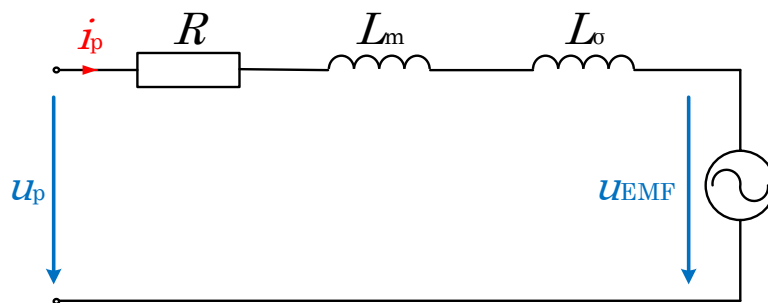


Figure 1.5: Equivalent circuit of a single-phase BLDC motor [20].

Essentially, BLAC and BLDC motors differ in terms of the shape of the back-EMF and phase current as well as the number of phases energized simultaneously. As shown in Figure 1.6 (a), BLAC motors have sinusoidal back-EMF and current waveforms to produce constant output torque (three out of three windings are energized). On the other hand, as shown in Figure 1.6 (b), BLDC motors have a trapezoidal back-EMF and therefore require rectangular current waveforms to produce constant output torque (two out of three windings are energized). BLDC motors tend to produce more audible noise than BLAC motors caused by the rectangular-like current waveforms and hence high di/dt . The commutation in BLDC motors is sectioned in six 60 electrical degrees segments causing a torque ripple because the current slope of the incoming and outgoing phases differ. BLAC motors have smoother current waveforms and hence produce less torque ripple.

However, BLAC motors are more expensive than BLDC motors because their control and position sensing is more complex [21].

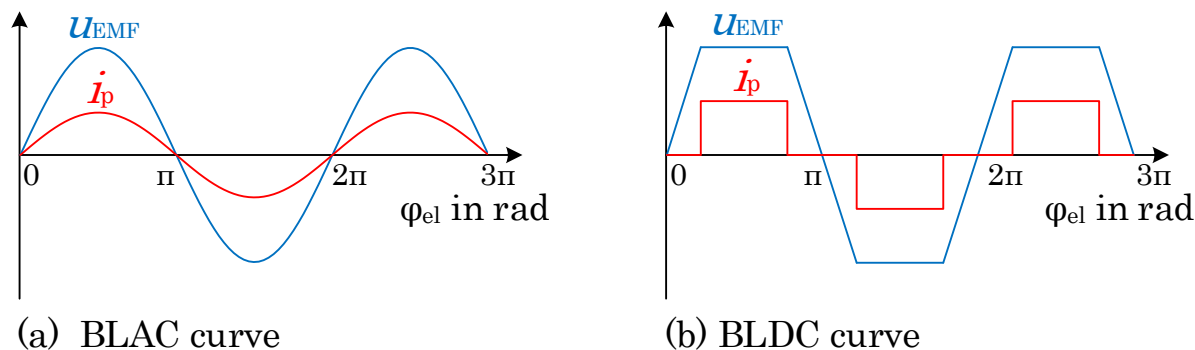


Figure 1.6: Idealized current and back-EMF waveforms of a BLAC (a) and a BLDC (b) motor [19, p. 186].

Basically, motors are driven by different voltage waveforms, amplitudes and frequencies. A common control strategy is the **pulse wide modulation** or **PWM**. This technique generates the desired current waveform simply by switching the semi-conductors on or off. As a result, the motor voltage will get either high or low. The pulsed voltage is applied to the motor where the inductance and resistance of the winding cause the current to rise exponentially (the winding acts like a filter to current harmonics). The current can be controlled by varying the PWM's duty cycle, which is defined as the ratio of the on-time t_{on} and the switching period T ($T = t_{on} + t_{off}$) [22, p. 73]. This technique is necessary to control the desired rectangular or sinusoidal currents of BLDC and BLAC motors, respectively. Low-cost BLDC motors, designed for only one operating point, are often operated using **square wave commutation**, which simply generates one current impulse every 180 electrical degrees. A major benefit is the low switching frequency and accordingly low switching losses but the current waveform cannot be controlled. In fact, it results according to the difference between the applied constant phase voltage and the back-EMF. The current waveform of such a BLDC motor has two values of interest, A and B, see. Figure 1.7. For an optimal operation, these values should be approximately the same to yield the desired rectangular current waveform, which can be influenced by the turn-on angle θ . This switching strategy shows reduced electromagnetic emissions due to the reduced switching frequency [23, p. 1123 - 1127], [24, 1937 - 1939], [25].

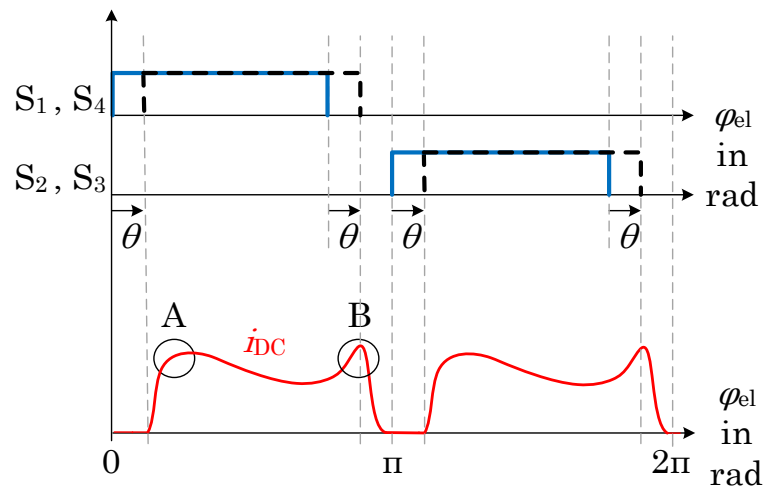


Figure 1.7: Generic current waveform for square wave commutation indicating the switching [23, p. 1123 - 1127], [24, 1937 - 1939].

A further distinction is made between the stator winding. The most used realizations are the **single-** and **three-phase winding** stator. Figure 1.8(a) shows a single-phase BLDC motor in which one wire is alternately wound in clockwise and counterclockwise directions around the salient stator poles. Thereby, a current in the winding generates four magnetic poles (N-S-N-S) in the air-gap. The stator has an asymmetric air-gap to facilitate the starting [26, p. 8]. An advantage of this topology is the reduced number of power electronic switches. The three-phase stator has three windings, which are connected in a star or delta, which is illustrated in Figure 1.8 (b) [17, p. 1123 - 1124].

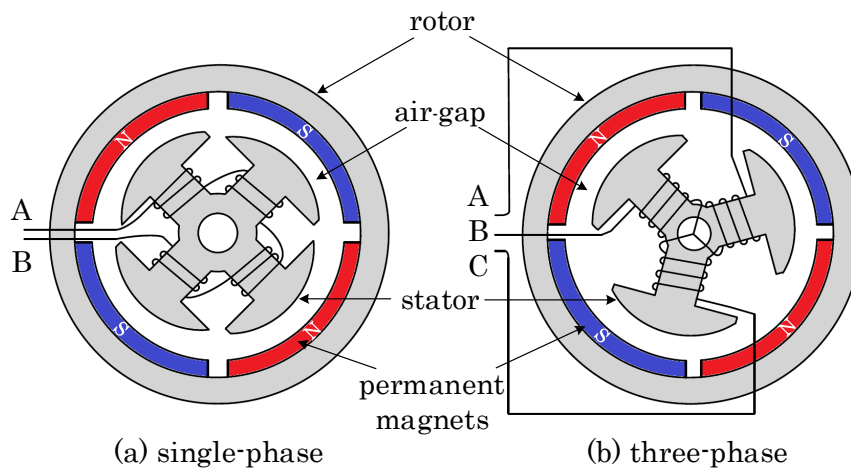


Figure 1.8: Simplified comparison of the construction between a single-phase (a) and a three-phase (b) stator [17, p. 7].

The function of the motor is based on the attraction and repulsion of unlike and like magnetic poles, respectively. The current through the coil produces a magnetic pole, which attracts the closest opposite pole of the rotor. BLDC motors usually use power electronic switches like MOSFETs for the commutation. These switches are usually connected in an H-bridge for single-phase motors and in a three-phase bridge inverter for three-phase motors. Usually the high-side switches are used for the pulse wide modulation, while the low-side switches are turned on. Special control strategies use both the high-side and low-side switches for the chopping. The easiest way to control a **single-phase motor** is to track the position with one hall sensor. If the north-pole of the rotor is passing, the sensor goes high (and vice versa). A **three-phase motor** needs three Hall sensors to track the position. The sensors are located every 120 electrical degrees. Combining the signals, it is possible to locate the rotor position every 60 degrees. Hence it takes six steps to complete a full electrical rotation. If it is not possible to track the position of the rotor with the Hall sensor, **sensorless** commutation strategies can be used, e.g., back-EMF sensing. A disadvantage of this technique is that the rotor needs a minimum speed to get the feedback signal [17, p. 7 - 8].

There are two established winding topologies for **single-phase BLDC** motors:

- **unifilar** winding
- **bifilar** winding

In principle, a **unifilar** winding has only one wire wound on the salient stator poles as discussed in the context of Figure 1.8 (a). To generate non-zero average output torque, it is necessary to alternate the current polarity. In case of **bifilar** winding, two wires are wound simultaneously around the salient stator poles indicated in Figure 1.8 (a). The start and end connections of one wire must be interchanged to obtain coupled coils of opposite polarity [26, p. 8]. The schematic circuit of both designs (indicating inductances only) is illustrated in Figure 1.9.

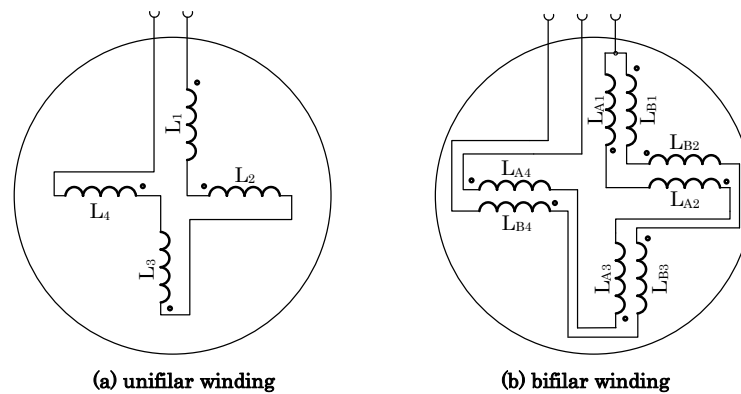


Figure 1.9: Schematic circuit of a single-phase BLDC motor with (a) unifilar [26, p. 21] and (b) bifilar winding [20, p. 3]

Besides the design differences, their control strategies differ as well, which is explained in Figure 1.10.

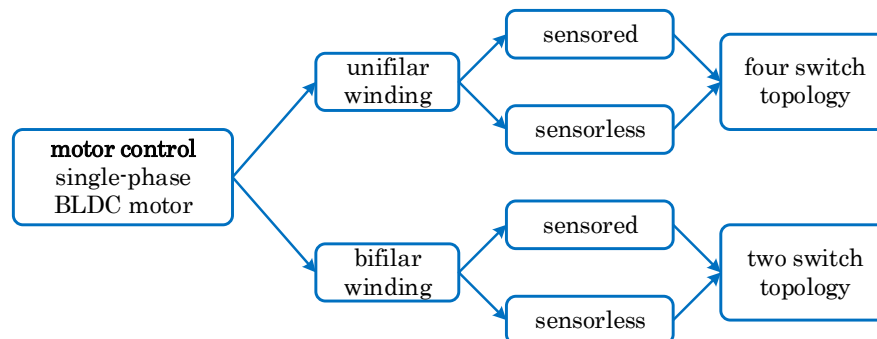


Figure 1.10: Possible control techniques of a single-phase BLDC motor [26, p. 65].

Figure 1.11 represents the inverter circuit for a unifilar (a) and a bifilar (b) single-phase BLDC motor.

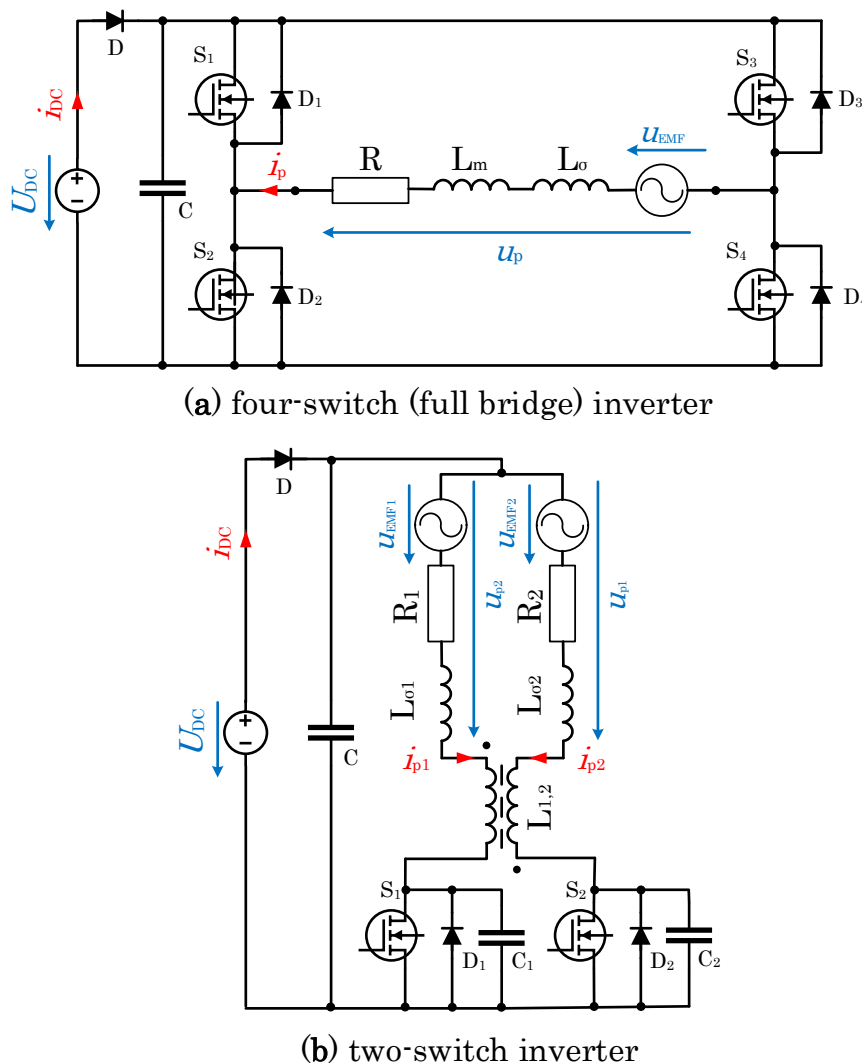


Figure 1.11: Inverter circuit of a single-phase BLDC motor: (a) full bridge for unifilar and (b) two-switch inverter for bifilar winding [26, p. 66 - 71].

The entrance network of both typologies in Figure 1.11 is equivalent. It consists of the dc supply voltage U_{DC} , the diode D , which is a reverse polarity protection, and the capacitor C , which ensures a stable and smooth voltage.

Figure 1.11 (a) shows the inverter circuit to drive the **unifilar** winding of a single-phase BLDC motor. The four switch topology has to be chosen, because the current flow must be bidirectional. The unifilar winding can be modeled by the stray inductance L_{σ} , the main inductance L_m and the resistance R , which represents the

copper losses. U_{EMF} represents the induced voltage due to the changing field of the rotating magnets. Basically, full bridges consist of four power electronic switches S_1 to S_4 and four diodes D_1 to D_4 . The task of the switches is to convert the dc power to ac power. The diodes provide free-wheeling paths for the current while the switches are turned off [23, p. 1124] [26, p. 68 - 70].

Figure 1.11 (b) shows the inverter circuit, which drives the **bifilar** winding of a single-phase BLDC motor. This motor design can be illustrated by two equal parallel unifilar phases, which is shown in Figure 1.5. The sub-phases 1 and 2 of the bifilar winding can each be modeled like a unifilar winding. Depending on the rotor position, which is detected by a Hall effect sensor, the bifilar winding is energized by the use of power electronic switches S_1 and S_2 respectively. It is important to note, that due to the extremely good coupling of the bifilar winding the main inductance $L_{1,2}$ can be modeled as a transformer. During the commutating process, magnetic energy can dissipate as a free-wheeling current in the other phase, which results in a negative spike. An advantage of this topology is the reduced number of power electronic parts, which is possible, because the current flow is unidirectional. Disadvantageously, a bifilar winding requires double the amount of copper only 50% of which is utilized at a time [2, p. 2 - 9], [26, p. 68 - 70].

1.4 Characteristics of small electric drives

In general, it is not possible to simply scale a drive geometrically and receive the desired properties. For example, small components are more vulnerable to manufacturing tolerances. In addition, the relative air-gap is much larger than, e.g., in integral horsepower drives. A larger air-gap generally results in a lower flux density (for the same excitation effort) and hence magnetic forces, which is advantageous regarding of the sound development. Further, the small construction size poses a rather poor sound radiator with rather high resonance frequencies. Due to the small drive's geometry these motors have a low inductance L and a high resistance R . Furthermore, the high resistance leads to a low efficiency η . Since sub-fractional hp motors are essentially low-cost applications, weak magnets are usually used, which results in a sub-optimal motor behavior. An increased occurrence of torque ripple, for example caused by the cogging and commutation torque, is typical for these drives. The vibration behavior is also strongly influenced by the installation location and mounting.

1.5 Subjective sound sensibility

The human ear can detect sound waves with frequencies between 16 and 20.000 Hz. This range of audibility does not follow a linear curve, in fact. a minimum of perceived intensity is existent. This level is called the **threshold of audibility**, which is different for each frequency (i.e., the human ear is less sensitive to low frequencies and more sensitive to high frequencies). The upper limit of audibility is the **threshold of pain**. This **zone of audibility** was created by a statistical evaluation, which is shown in Figure 1.12 [27,28].

Some examples for typical sound power levels are [27, p. 3]:

- low voice: 40 dB
- normal conversation: 55 dB
- heavy city traffic: 92 dB
- jet plane take-off: 150 dB

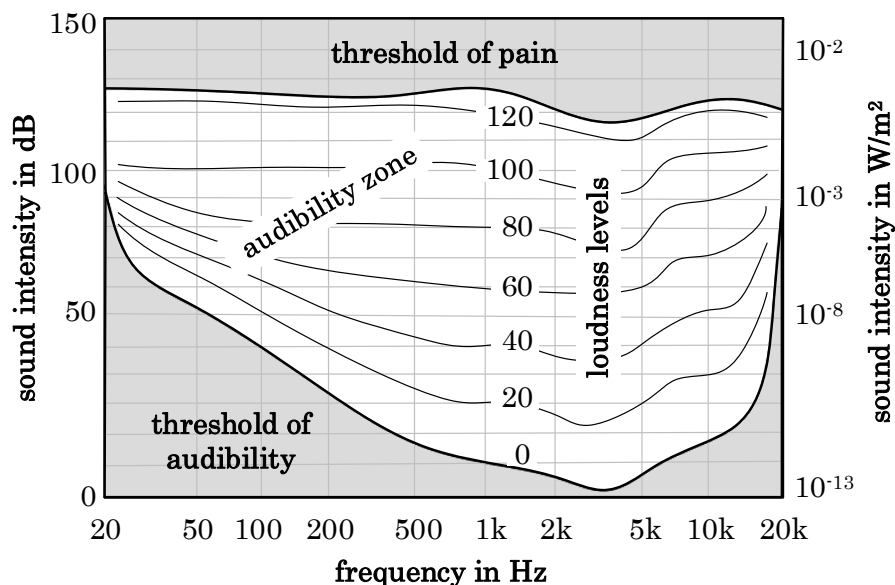


Figure 1.12: Subjective human sound perception as a function of frequency [27, p. 3].

A unit for the acoustic perception is the volume in phon. Over a volume of 40 phon an increase of 10 phon is perceived as a doubling. To receive a linear connection of

the subjective sound sensibility and the volume in phon, the loudness N in sone can be used. N doubles at every 10 phon and allows the curve to be linear [28].

With respect to automotive acoustics, it is important to distinguish the following:

- **actuating** noise
- **disturbing** noise

If the function is activated by the driver, a sound may be perceived as a confirmation (e.g., window lifter) and is hence classified as actuating noise. The noise of functions which are activated automatically are rather perceived as disturbing (e.g., fuel pump or engine fan). Also the localization and a noise corresponding to the expectations have an effect on the human perception [1, p. 396].

1.6 Air-borne sound measurements

Air-borne sound measurements are performed using microphones. The easiest way to perform this measurement is to use a microphone and a computer with audio software. Depending on the requirements, there are different measurement systems, which are usually connected with high effort and costs. The basics of the two most established measurement systems are discussed below.

Array measurements allows to record the sound emissions of a specific area, see Figure 5.2. With a high resolution it is possible to precisely determine the noise-forming areas of a component. In order to make this noise localization possible, a run-time comparison of the microphone signals can be carried out. In addition, it is possible to overlap the resulting visualization, which is obtained from the microphone array, with an image file of the measurement object to simplify the allocation of the noise areas. The biggest challenge using this method is the data processing, because an array often contains more than 120 microphones with a sampling rate of 192 kHz. Attention should be paid to the limits of this method. By measuring small objects for example, the resolution has to be very small [6, p. 379-380].

Besides the frequently used microphone solutions, sophisticated systems are existent to record the subjective noise perception. The **artificial head** is a solution with two microphones in the ears of a dummy, see Figure 1.13. This method allows to measure the subjective impressions of a human, caused by the reflections on the head and shoulders.



Figure 1.13: Artificial head.

1.7 Structure-borne sound measurements

Structure-borne sound measurements are most commonly performed using accelerometers because the forces can easily be calculated knowing the object mass ($F = m \cdot a$). (Alternatively, distance or velocity measurements can be used but the incorporated derivative calculation ($F = m \cdot \dot{v}$ or $F = m \cdot \ddot{s}$) is often problematic in case of present signal noise.) Another advantage of **accelerometers** is the wide range of sensors and the low price. In addition, devices with up to three orthogonal measuring directions are available [6, p. 380]. Measuring very light objects is yet challenging as the mass of the sensor should not exceed approximately 10% of the measured object's mass [29, p. 12]. It should be noted, that miniature sensors with a mass of 0.4 g are available [30]. If the mentioned condition cannot be met, a non-contact measuring method, e.g., using a **laservibrometer**, may be more suitable to measure small light objects. This method has no backlash and no change of the object's mass. Further, the measuring point would be very small. A disadvantage is the high price, which is up to 20 times higher in comparison to an accelerometer or a microphone [6, p. 380].

1.8 Noise assessment

Usually, an increased emission of noise leads to an increasing wear which could decrease the machine's durability. The enhanced noise generation obviously occurs in case of a material defect. In most other cases vibrations produce noise which

concurrently leads to a higher material stress. Figure 1.14 illustrates the flow process of noise assessment. This flow chart equally accounts for solving simple noise problems and also for series noise tests [6, p. 381].

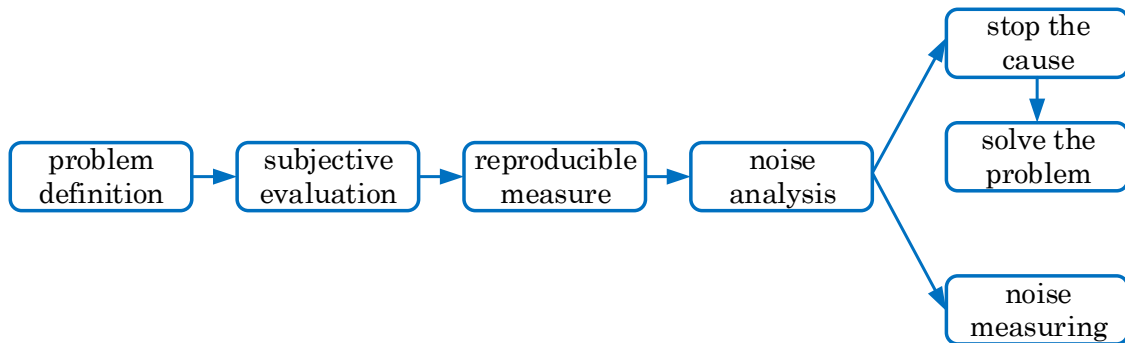


Figure 1.14: Flow of noise assessment process [6, p. 381].

In the following each individual step from Figure 1.14 is described. An important yet often underestimated aspect, even though it is the most important one relating to the communication with different sections, is the detailed **problem definition**. This description should include items such as:

- rough noise description
- operating condition (e.g., speed, temperature, torque)
- mounting conditions

Basically, a more accurate description will simplify a first estimation of the problem. In many cases the emitted noise has no impact on the function, but it is perceived as disturbing. If legal requirements exist (e.g., work safety), the approach is described in the standards (e.g., DIN 45635 / DIN EN ISO 1680). If no standards exist, the problem is more difficult [6, p. 381 - 382].

To evaluate the **subjective noise** limits, it is necessary to classify a few selected testing examples. The recording and storage of the data is as important as the evaluation. In order to solve this problem, a beneficial method of measuring is the artificial head, see Figure 1.13. Thereby, the subjective hearing impressions are portrayed without a secondary treatment of the data. This problem goes hand in hand with the subjective noise sensibility of the human ear, see Chapter 1.5. The

psychoacoustic signal analysis follows no physical laws, but considers the noise perception of the human ear. The goal is to find a relationship between the human perception and physical quantities [6, p. 382 - 385].

In order to make a meaningful analysis possible, it should be ensured that the measuring is **reproducible**. The reproducibility ensures similar measurement results, without dependence on the auditor. Therefore calibrateable measurements must apply. Also the installation type has to be identical, because of the change of system components if the measuring is made in the application [6, p. 382 - 384].

To be able to properly **analyze** the measured data, it is necessary to know all mechanical and physical boundary conditions. Basically, rotating machines have three main frequency parts:

- speed proportional parts
- non speed proportional parts
- resonances caused by component natural frequencies

For example, a startup experiment allows visualizing the three different parts. In case of a noise problem, it is irrelevant which measuring method is used. For a vibration problem the usage of accelerometers is efficient [6, p. 384]. A typical composition of the noise sources depending on the rotation speed of rotating machines is illustrated in Figure 3.2.

Chapter 2

Fan drives

2.1 Introduction

In general, fans are fluid machines which move and/or compress air. The main fansystem components include the motor drive, the fan blades, and the housing. The motor drive ensures the rotation, the fan blades move the air, and the housing determines the flow direction as well as the pressure increase. Main drive technologies are the brushed direct current (DC) motors, alternating current (AC) line-start motors, and electronically commutated (EC) motors [31, p. 6].

2.2 Fan type overview

Depending on the desired direction of the airflow and pressure, it is important to use the right fan type. The main fan types along with their respective airflow directions are illustrated in Figure 2.1.

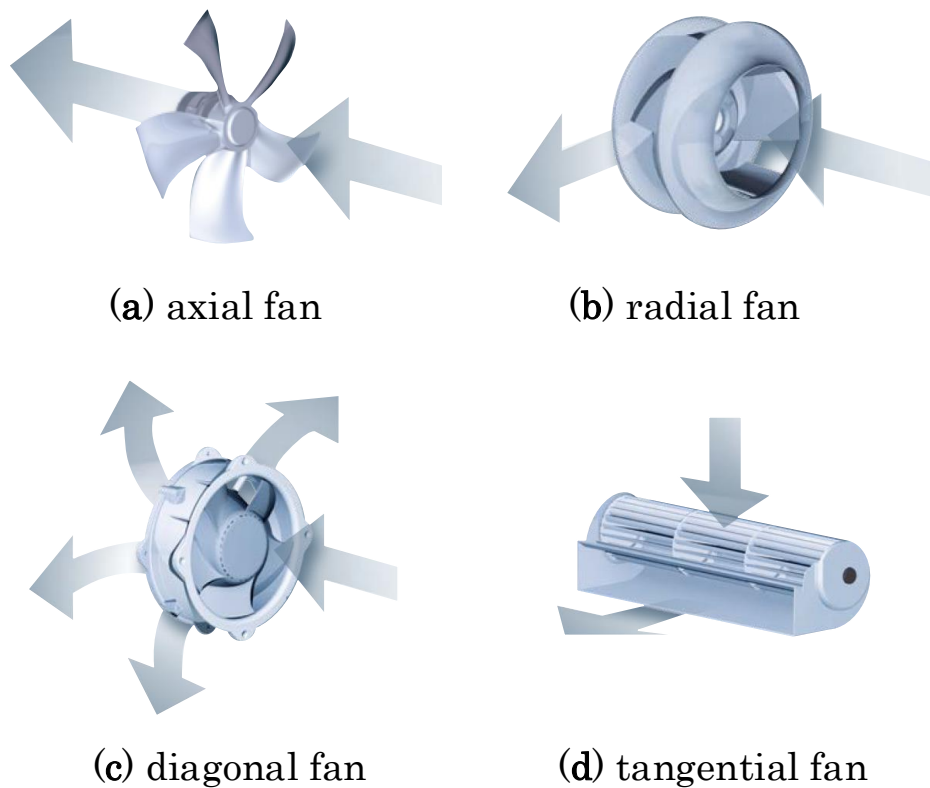


Figure 2.1: Different fan types with the airflow direction [31, p. 6].

Fans are named after their air in- and outflow directions. In Figure 2.1 (a) an **axial fan** is illustrated, in which the in- and outflows are parallel to its axis. Figure 2.1 (b) presents a **radial fan**, which is often called **centrifugal fan**. Its name is based on the fact that the inflow is parallel to the fan axis and the outflow is in the radial direction. (The axial and radial fan types are described in detail in Chapters 2.3 and 2.4.) Figure 2.1 (c) presents a **diagonal fan**, which is a mix of an axial and a radial fan. The inflow is in the axial direction but, since the housing and blades are conically shaped, the air flows out diagonally. Under consideration of the operating conditions, diagonal fans are located between the axial and radial ones. They are the best choice, if axial fans provide too little pressure and radial fans too low airflow. The **tangential blowers**, shown in Figure 2.1 (d), consist of drum-shaped impellers. Both the air inflow and outflow run radially. This type provides a high airflow

and a low back pressure, having a rather poor efficiency. The main advantage is the extremely low noise generation. Thus, it is used for applications with low air performance like indoor units of air-conditioning systems [31, p. 6], [32, p. 5].

For a **given fan size** and rotating **speed**, Figure 2.2 shows the relationship between the volume rate and the air pressure. Axial fans are characterized by a high volume rate at low air pressure, radial fans have a low volume rate at high air pressure, and diagonal fans are somewhere in between [32, p. 5].

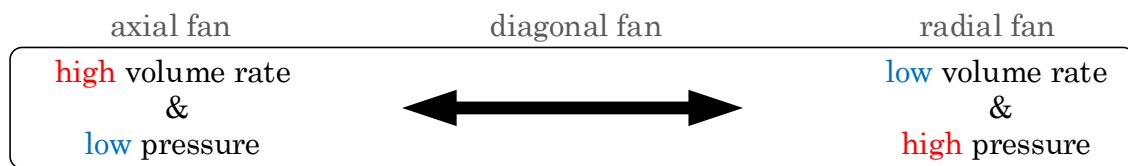


Figure 2.2: Aerodynamic relationship between the volume rate and the air pressure of the different fan types of the same size and speed [32, p. 4].

A possibility to influence the volume rate and air pressure of axial fans is to place them in different configurations. The volumetric flow rates add up if the fans are placed in **parallel**, while the pressure remains unchanged. (When two identical fans are placed in parallel the flow rate is doubled at the same pressure.) Conversely, the air pressures add up if the fans are placed in **series**, while the volume rate remains unchanged. (When two identical fans are placed in series, the air pressure doubles but the flow rate remains unchanged). In some applications a combination of parallel and series configurations will be used, this is the so called push-pull system [33].

In order to find the most suitable fan for a given application, it is an advantage to know the typical fan curves illustrating the relationship between the back pressure P and the volume rate q (see Figure 2.3 for typical fan curves). They provide the user with an overview of the optimum operating range so to pick the best option for the given system. An example for an axial fan is shown in Figure 2.4, where the intersection of the fan and system curves determine the operating point.

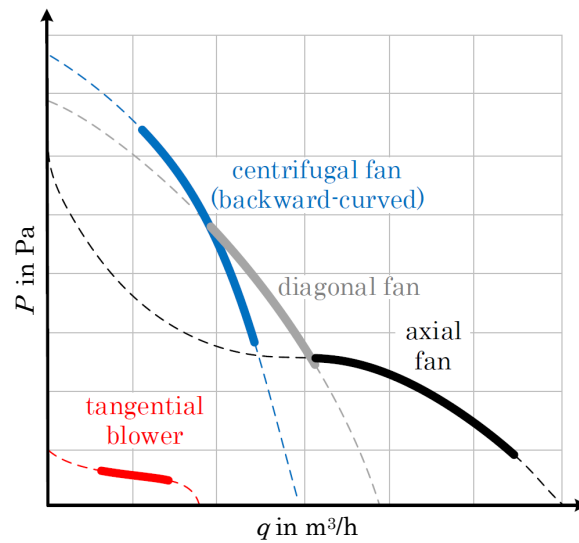


Figure 2.3: Typical fan curves and their optimal operating range [31, p. 7].

The fan curves are determined on a test stand and are usually provided by the manufacturer. Furthermore, it is possible to measure or calculate the system curve. For a different operating point, it is inevitable to change either the system curve or the fan curve [32, p. 8].

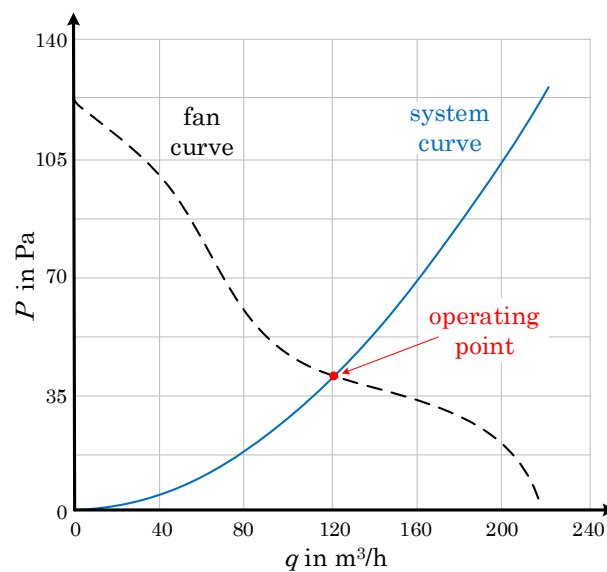


Figure 2.4: Determination of the fan's operating point [32, p. 9].

2.3 Axial fans

As previously mentioned, axial fans are characterized by low air pressure and high volume rate. The advantages of axial fans are their flat design, a low noise level, and a high efficiency. As mentioned before, axial fans provide a high volume rate at a low pressure. The fundamental operation is similar to the propeller of an airplane. However, an operation without the housing comes with a reduction in the performance of up to 15 percent and the airflow control is lower as well. In most applications, axial fans operate with a housing. Some axial fans allow an operation in both airflow directions. In general, the output power of the fan increases with increasing back pressure. Therefore they are often used in free air operation.

Axial fans can be implemented with inner- or outer-runner motor. In inner-runner designs, the impeller is mounted onto the shaft of the motor which increases the axial length of the fan and hence its size. In case of an outer-runner design, the blades are directly mounted onto the rotor, saving space (see Figure 2.5). In addition, outer-runner motors have higher inertia than inner-runner ones (due to their larger air-gap diameter), which is beneficial for a smooth operation. For these reasons, it is the most common design [31, p. 5-7], [32, p. 4-28], [33].



Figure 2.5: Rotor of an axial fan with seven blades.

Comparing the axial fan in Figure 2.5 with the radial fan in Figure 2.6, it is obvious that an axial fan generally has many fewer fan blades than a radial fan, which is also reflected in the emitted noise.

2.4 Radial fans

As previously mentioned, radial fans are characterized by high air pressure and low volume rate. The two main embodiments of radial fans are impellers with backwards-curved and forwards-curved blades, with respect to the direction of rotation. A special property of radial fans with backward-curved blades is that they operate with or without a housing. An advantage of the operation with housing is the exact orientation of the airflow. Radial fans with forward-curved blades can only operate with a scroll housing to built up the pressure. The forward-curved blades are often referred to as drum impellers. Furthermore, radial fans are rather quiet as the blade passing noise decreases with increasing number of blades, resulting in a low-amplitude broadband noise [31, p. 5-7], [32, p. 4], [33].

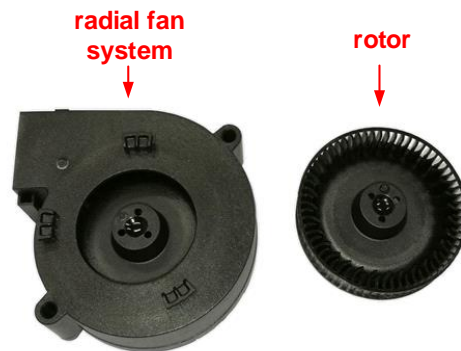


Figure 2.6: Radial fan with forward-curved blades and scroll housing.

Comparing the radial fan in Figure 2.6 with the axial fan in Figure 2.5, it is obvious that a radial fan generally has many more fan blades than an axial fan, which results in a decreasing blade passing noise and results in a low-amplitude broadband noise.

2.5 Comparison

It is important to take the application specification and thus the system curve into account when selecting a suitable fan, as shown in Figure 2.4. Furthermore, Figure 2.3 gives a good overview of the optimal operating range of the different fan types. The back pressure and the volume rate of axial fans can also be changed with so-called push-pull systems, i.e., parallel or series installation of axial fans. It must also be

considered whether directed airflow is needed or the emitted noise level is important. Axial fans basically offer a high air volume with low back pressure. However, noise and power consumption increase very quickly when the back pressure rises. Radial fans generally offer a low air volume at high back pressure. Due to the high number of fan blades, there is no distinct blade passing noise. Instead a broadband noise with reduced amplitudes occurs, which is usually perceived as more pleasant. Diagonal fans are a combination of radial and axial fans. Tangential fans provide a high airflow at a low back pressure. An advantage is the very low noise level, however the efficiency is poor. This means that these fans are used in applications that require high airflow at low noise levels, such as indoor air conditioning units.

Chapter 3

Sources of noise and vibrations in electrical machines

3.1 Introduction

Depending on the application, the noise of an electrical machine may be another important factor besides efficiency and output power. Noise generation is clearly a multi-disciplinary topic.

The following three sources of noise and vibration are distinguished.

- **electromagnetic** source
- **mechanical** source
- **aerodynamic** source

These sources can either directly or indirectly lead to noise, as illustrated in Figure 3.1. In general, the **electromagnetic** and the **mechanical** sources generate forces, which act on the motor, stator housing and other construction elements. Depending on the mechanical transfer function, these forces can cause vibrations, i.e., structure-borne noise, which in turn can result in air-borne noise at a vibratory surface, a form of indirect noise generation. On the contrary, **aerodynamic** sources generate noise directly, due to air turbulence and air resistance [34, p. 490 - 495], [35, p. 49 - 58]. An important aspect is that aerodynamic noise and mechanical noise are both proportional to the speed. The electromagnetic noise strongly depends on the load condition and changes thereof [36, p. 96]. Figure 3.2 shows the percentage sound power generation of the described noise components for rotating electric machines as a function of the rotational speed.

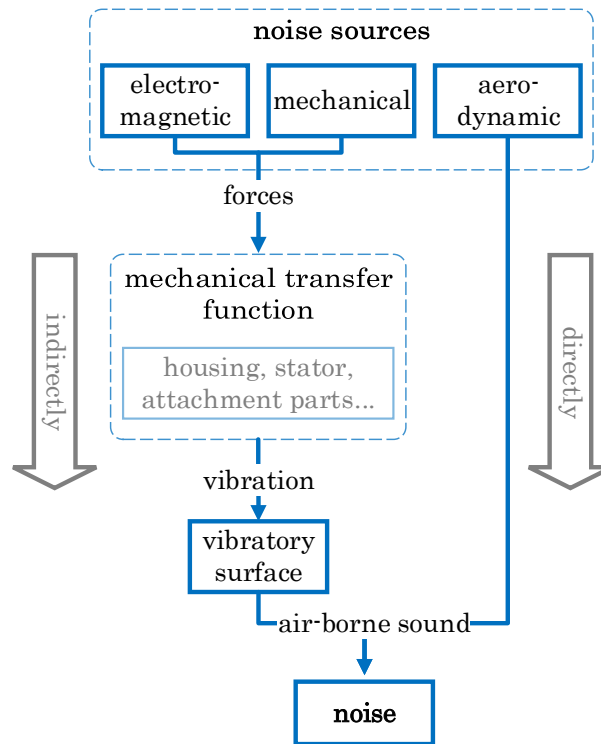


Figure 3.1: Sources of noise and vibration [35, p. 54].

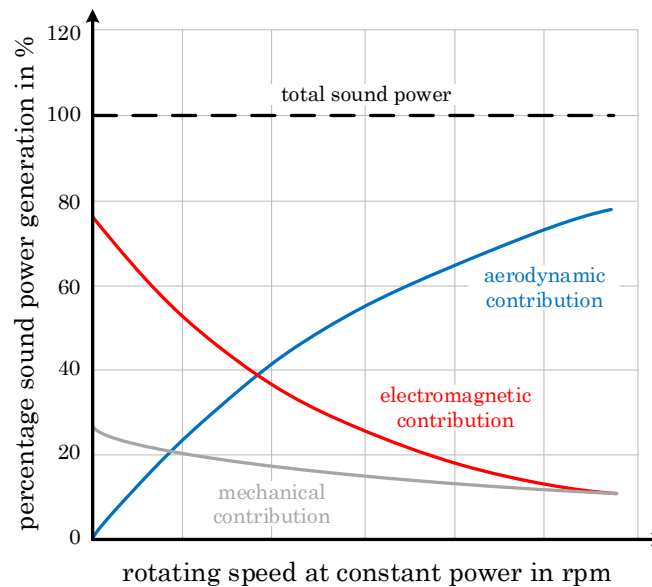


Figure 3.2: Typical composition of the noise sources depending on the rotational speed for constant output power [37, p. 693].

It is important to note that Figure 3.2 only shows the qualitative behavior. Nevertheless, it gives an idea about the composition of different noise contributions [37, p. 693].

Basically, the dimensions of an electric machine are a compromise between power, heat development, and noise emission. The efforts to increase drive efficiencies in recent years have led to altered percent sound power generation. In 1950, 0.1 - 10 MW drives from Siemens had a percentage noise distribution of 45 % electromagnetic, 45 % aerodynamic and 10 % mechanical. In 1975, the same drive types had a percentage noise distribution of 20 % electromagnetic, 75 % aerodynamic and 5 % mechanical. This change was achieved by intensive research on the reduction of electromagnetic noise and the increase of machine utilization in the years between. This shows that the cooling need of the drives increase with the reduction of the electromagnetic noise and the increasing of machine utilization. In short, it can be concluded that the electromagnetic portion has decreased while the aerodynamic portion has increased [34, p. 493].

3.2 Mechanical sources

The effect of the mechanical source is similar to that of the electromagnetic one. Figure 3.1 shows the mechanical source that generates forces which could develop vibrations depending on the transfer function of the mechanical system (e.g., housing, stator, attachment parts). These oscillations are called structure-borne sound. If they arrive at a vibratory surface, audible noise is emitted, which means that the noise is generated indirectly. The common frequencies of the noise are calculated in Chapter 3.5. The main reasons for mechanical noise are **imbalance** of the rotating system, **bearing**, **gear unit** and **friction**. In general, slide bearings are less noisy than ball bearings. Also, precise manufacturing helps counter the generation of noise. In the case of imbalances, static and dynamic forces can occur depending on the ratio of rotor length and diameter is existent. If the length is smaller than the diameter only static forces occur with the first order, which corresponds to the mechanical speed per second. In case of a long rotor, dynamic forces may occur as well. To counteract this, balancing in two plains can be of advantage. In case of mechanically commutated motors, the periodical transition of the carbon brushes between commutator ribs may cause an excitation frequency f_{rib} [1, p. 397], [6, p. 376 - 377], [35, p. 54 - 57].

3.3 Electromagnetic sources

To be more specific on the **electromagnetic** source, see Figure 3.3. Basically, the electromagnetic noise is often caused by vibrations, which arise from magnetic forces [6, p. 378 - 379]. Caused by vibrations of electromagnetically affected parts, an electromagnetic sound can be produced. These forces are transferred through the yoke as well as the machine housing and foundation, whereby these vibrations can develop in two different shapes:

- **radial** or **normal** forces (caused by magnetic pull)
- **tangential** forces (caused by torque fluctuations)

As long as the vibrations occur in the structure (e.g., housing, attachment parts) it is called **structure-borne sound**. If the vibrations arrive at a vibratory surface, **air-borne sound** is emitted [34, p. 490].

The forces which occur in the radial direction can lead to a deformation of the stator into corresponding modal forms. The order number r indicates the type of deformation. The lower order modes are usually the most critical ones [mode 0 (pure pull), mode 1 (shaking forces), mode 2 (bending), mode 3 (triangular or hexagonal node oscillation), and mode 4 (four node or eight node oscillation)] [34, p. 494 -495].

Remark: The magnetic pull f is proportional to the square of the magnetic air-gap flux density (B_δ) and μ_0 is the permeability of free space.

$$f = \frac{B_\delta^2}{2 \cdot \mu_0} \quad (3.1)$$

Basically, tangential forces form the desired torque. However, there can also occur non-constant forces in tangential direction (**torque fluctuations or ripples**) [34, p. 490]. The torque fluctuations are a superposition of **cogging** and **operation torque ripples**. In permanent magnet motors, the cogging torque ripple is an issue which can be reduced by improving the motor design. The operation torque ripple can be classified in commutation and inherent torque ripples. The inherent torque ripples are generated by non-ideal back EMF, while the commutation torque ripple is generated by the difference between the rising and the falling rates of the currents [6, p. 378 -379], [38].

Remark: All these occurring time-variable forces discussed above, build an integrated force which produces the desired torque as well as undesirable deformations and oscillations [6, p. 378].

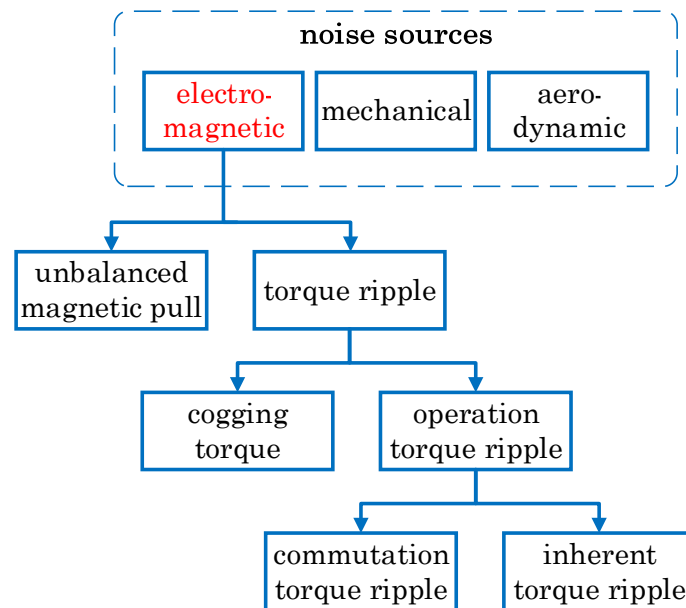


Figure 3.3: Electromagnetic sources [38].

Furthermore, semiconductors are able to generate noise due to the switching. This noise emission depends on the kind of semiconductor, temperature, frequency and other parameters. In [39], a unified noise characterization technique for MOSFET's is described.

Also, the **magnetostriction** is able to generate vibration and noise. This effect is a common issue of ferromagnetic materials like steel. It describes the variation of length and shape of a material, when exposed to a magnetic field. Depending on the material characteristic, the effect is more or less pronounced. For example iron, nickel, and cobalt alloys have an expansion of up to $30 \mu\text{m/m}$. In contrast semiconductor iron alloys exhibit an expansion up to $2000 \mu\text{m/m}$ [40, p. 278 - 279]. Basically, magnetostriction is a common issue of transformers where this effect finds expression in double the frequency of the magnetic field (e.g., the 100 Hz humming of a 50 Hz transformer). This magnetostrictive expansion increases more than linearly with induction. In addition, cold-rolled steel in the preferred direction exhibit about one third of the magnetostrictive extension of hot-rolled steel at the same induction [41, p. 24 - 25]. Caused by the small stator dimensions and the air-gap, this source does not significantly contribute to the whole noise spectrum [35, p. 62], as the measurements in Chapter 4.4 show.

In general, the electromagnetic noise strongly depends on the magnetic forces in the air-gap. The normal (or radial) forces are proportional to the square of the air-gap flux density B_δ [see 3.1]. It has been found that the air-borne sound power is proportional to B_δ^4 . Hence, noise can be reduced by reducing B_δ . This can essentially be realized by using weaker magnets or increasing the air-gap. An increased air-gap can be implemented in two ways. One is to use a smaller rotor for a given stator and the other is to increase the stator bore diameter for a given rotor if space permits. However, the output power (P_{out}) and torque (T) are reduced as well [36, p. 105].

Remark: Due to the relatively large air-gap, dictated by mechanical tolerances, and the cost-related usage of rather weak magnets, the potential to reduce noise by lowering the air-gap flux density in small electric motors is very low.

Finally, an **example** on the field of electromagnetic noise. The cogging torque of electric machines can be a source of noise [1]. Reference [42, p. 153] presents an outer-rotor motor with sintered segment NdFeB magnets in which the cogging torque has been minimized by optimization of the magnet length and the stator pole shape. However, the remaining cogging torque caused unacceptable vibrations. This problem was solved by implementing recesses in the rotor bell in order to change the natural frequency thereof.

3.4 Aerodynamic sources

As illustrated in Figure 3.1 aerodynamic sources directly generate air-borne noise in the form of air turbulences. Besides broadband noise, which results from air flow through the air channel, ventilation drills or cooling modules, also tonal noise can occur. Figure 3.4 shows a generic noise spectrum of a fan drive [1, p. 398]. Especially the **blade passing noise** of axial fans and **interference noise** resulting from the interaction of the blades, struts, and the housing are distinct. The calculation of occurring frequencies is presented in Chapter 3.5. Detailed differences of the fan types are described in Chapter 2. The blade passing noise is a mono sound source, which is affected by the time variable mass flow. It is proportional to the fourth order of the flow speed and thus to the peripheral speed of the rotor. Furthermore, flow generated noise is a dipole source which is proportional to the sixth order. Because of this aspect, in practice the estimation of increasing sound power level due to increasing rotation speed is calculated with an average fifth order depending of the peripheral rotor speed and a first order depending of the fan surface [1, p. 399].

The calculation is a very complex process, it links the laws of fluid mechanics with acoustics. However, a contained mathematical description is not existent [35, p. 50].

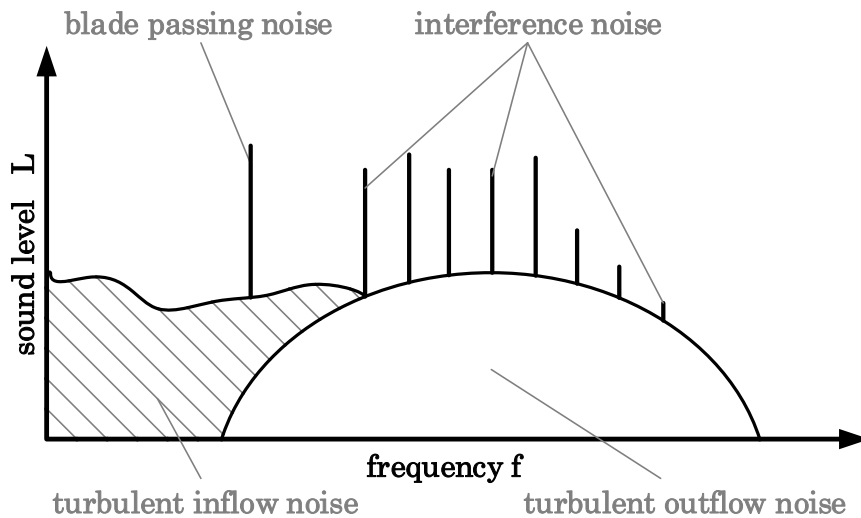


Figure 3.4: Generic noise spectrum of a fan [1, p. 398].

The turbulent inflow and outflow noise is a common issue of radial fans, which does not occur in axial fans. Further, the blade passing noise is a typical characteristic of axial fans, which hardly occurs in radial fans. Through interactions of the blades with struts, ribs, and housing interference noises can occur in both fan types [1, p. 399].

In Figure 3.5 some basic acoustic and aerodynamic correlations are illustrated. Figure 3.5 (a) shows the distance law, which describes the decrease of the fan sound level based on far field conditions (distance of one meter) by increasing the distance to the source. More accurately, the sound level in the far field conditions decreases by 6 dB every distance doubling. For example, if the space between the source and receiver is changed from 1 to 10 m, the sound power level will be nearly 20 dB lower.

The influence of the rotating speed on the generated noise is illustrated in Figure 3.5 (b). Based on the initial speed and the specified sound level of the fan, the sound level increases with increasing speed and vice versa (notice the nonlinear relationship). To estimate this relationship (3.2) can be applied.

$$L_0 - L_1 = 50\text{dB} \cdot \log \frac{n_0}{n_1} \quad (3.2)$$

- L_0 ... initial fan sound level
- L_1 ... sound level after speed change
- n_0 ... initial speed
- n_1 ... changed speed

For example, if a fan operates at 75 percent of its initial speed, the noise level will decrease by 6 dB.

The connection between the emitted sound level and the number of fans operating at the same time is shown in Figure 3.5 (c). Basically, the noise level rises by 3 dB at simultaneous operation of two equal fans. The number of fans is entered on the x -axis of the graph, and on the y -axis, the increase of the sound level can be determined. For example, if eight fans operate simultaneously the noise level increases by 9 dB based on the initial noise level.

Also the noise level will change by operating two different fans at the same time. Figure 3.5 (d) illustrates this relationship. The difference of noise levels, based on the initial values, is entered on the x -axis, and on the y -axis, the increase of the sound level can be determined. This value has to be add to the initial sound level of the louder fan. For example, if the initial noise level difference between the fans occurs is 4 dB, the total noise level will rise by 1.5 dB in addition to the louder one [31, p. 106 - 108].

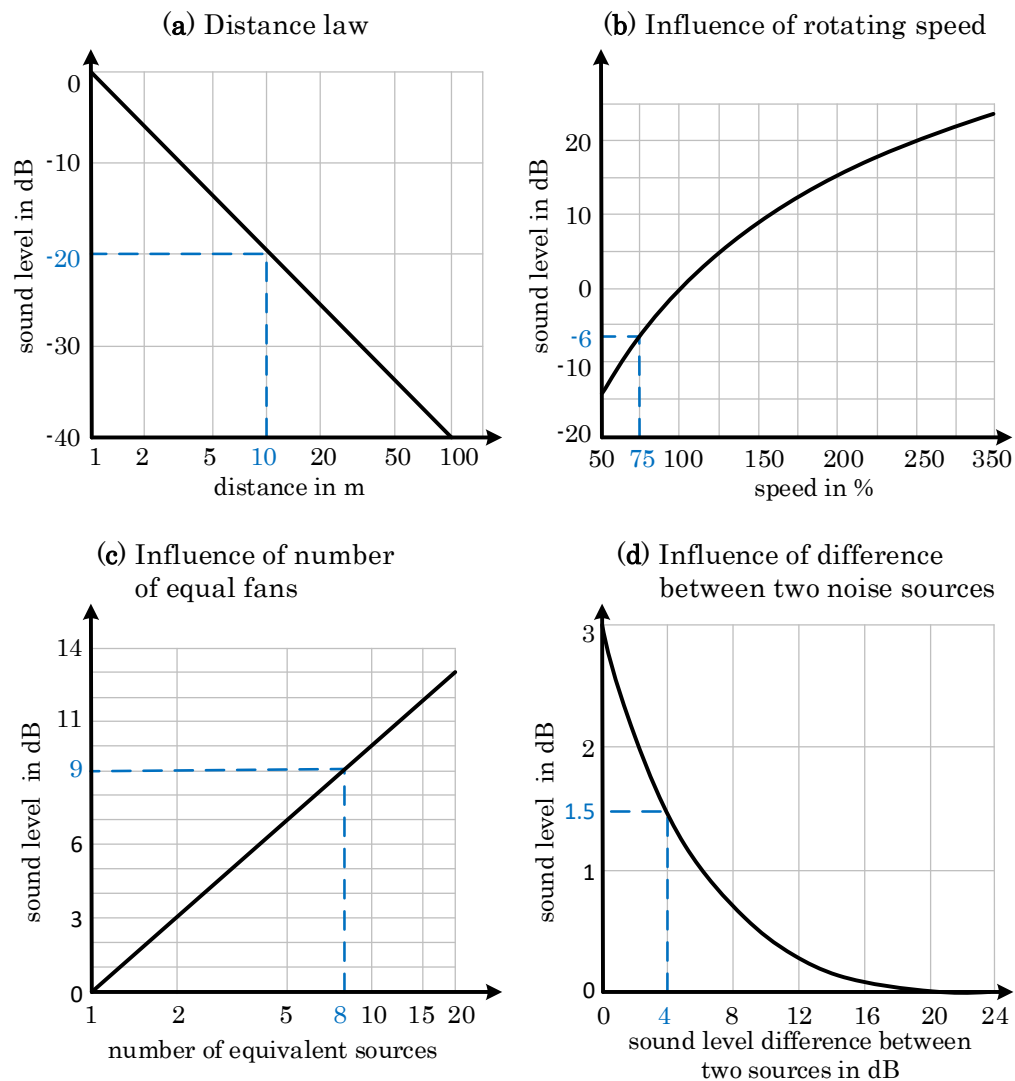


Figure 3.5: Basic acoustic and aerodynamic correlations [31, p. 106 - 108].

Finally, an **example** on the field of aerodynamic noise: High frequency whistling can occur in the suction area of radial fans. Often it is easy to eliminate this disturbing sound by applying a small impediment in this area [43, p. 93]. The European patent [44] provides more insights into that topic.

3.5 Excitation frequencies

As already specified in Chapter 3, three sources which generate noise and vibrations are existent. In the first part of this chapter the occurring frequencies will be

estimated. Usually, the base frequency is calculated and its multiple occur in the frequency range. The mechanical **shaft frequency** is defined as

$$f_n = \left(\frac{n}{60}\right), \quad (3.3)$$

where n is the rotation speed in rpm.

3.5.1 Mechanical excitation frequencies

In ball bearings, rolling elements, e.g., balls, are used between the inner and outer ring to reduce the friction. Depending on the type of construction and rolling elements, these can be loaded with axial or radial forces. The force direction depends on the contact angle, which is called α . Figure 3.6 shows the fundamental structure of a ball bearing, as well as the used variables.

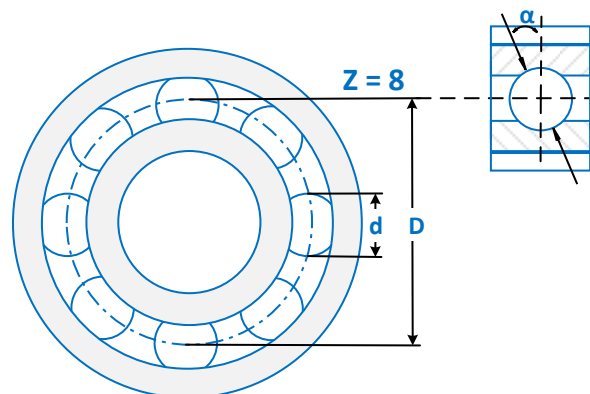


Figure 3.6: Geometry and definition of the used variables [45, p. 9].

- Z ... number of rolling elements
- d ... diameter of the rolling elements
- D ... pitch diameter
- α ... contact angle

The following frequencies may occur using a ball bearing. To calculate the **inner ring roll-over frequency** the shaft frequency f_n and the variables from Figure 3.6 are

needed [45, p. 10].

$$f_i = \frac{1}{2} \cdot f_n \cdot Z \cdot \left(1 + \frac{d}{D} \cdot \cos(\alpha)\right) \quad (3.4)$$

The **outer ring roll-over frequency** can be calculated similarly [45, p. 10].

$$f_o = \frac{1}{2} \cdot f_n \cdot Z \cdot \left(1 - \frac{d}{D} \cdot \cos(\alpha)\right) \quad (3.5)$$

The frequency generated by the **rolling units** during **over rolling** can be calculated as follows [45, p. 10].

$$f_r = f_n \cdot \left(1 + \frac{D}{d}\right) \cdot Z \cdot \left(1 - \frac{d}{D} \cdot \cos(\alpha)\right) \quad (3.6)$$

There are two cases in the calculation of the **cage rotation frequency** depending on the operating condition of the bearing [45, p. 10]: On the one hand in the case of the **rotating inner ring** and the stationary outer ring.

$$f_{c,i} = \frac{1}{2} \cdot f_n \cdot \left(1 - \frac{d}{D} \cdot \cos(\alpha)\right) \quad (3.7)$$

On the other hand in the case of the **rotating outer ring** and the stationary inner ring.

$$f_{c,o} = \frac{1}{2} \cdot f_n \cdot \left(1 + \frac{d}{D} \cdot \cos(\alpha)\right) \quad (3.8)$$

The **rolling ball frequency** can be calculated as follow [46, p. 3].

$$f_{bs} = \frac{D}{2d} \cdot f_n \cdot \left(1 - \left(\frac{d}{D}\right)^2 \cdot \cos^2(\alpha)\right) \quad (3.9)$$

The **roll over frequencies** which are linked to **irregularities** of the **rolling ball** can be calculated as follow [47].

$$f_{ibs} = 2 \cdot f_{bs} = \frac{D}{d} \cdot f_n \cdot \left(1 - \left(\frac{d}{D}\right)^2 \cdot \cos^2(\alpha)\right) \quad (3.10)$$

The frequencies which are linked to **irregularities** in the **ball cage** [46, p. 3]:

$$f_{bc} = f_n \cdot \frac{d_i}{d_i + d_o} \quad (3.11)$$

and the frequency due to **variation** of the **bearing stiffness** [46, p. 3]:

$$f_{st} = f_{bc} \cdot Z \quad (3.12)$$

Further mechanical frequencies may occur if a defect exists [35, p. 54-56]. Imbalance stimulates bearing to oscillate and generates a multiple of the shaft frequency. This occurs when there is **unbalance** f_{unb} or when the surface is **oval** f_{ov} , and can be calculated as follows:

$$f_{\text{unb}} = f_{\text{ov}} = k \cdot f_n \quad k = 1, 2, 3 \dots \quad (3.13)$$

The frequency which arises if the running surface has N_{notch} **notches**, can be calculated with (3.14):

$$f_{\text{notch}} = N_{\text{notch}} \cdot f_n \quad (3.14)$$

If the shaft **orientation** is not exact, the frequency f_{ori} can be occur.

$$f_{\text{ori}} = 2 \cdot f_n \quad (3.15)$$

If a **mechanical commutating** is existent, the following frequency may occur caused by periodical transition of the carbon brushes and the commutator ribs (z_r is the ribs number of the commutator) [6, p. 377].

$$f_{\text{rib}} = f_n \cdot z_r \quad (3.16)$$

3.5.2 Aerodynamic excitation frequencies

The calculation of the **aerodynamic** frequencies will be discussed in the following [1, p. 399], [35, p. 54-56]. Usually, the most dominating aerodynamic source in axial fans is the blade passing frequency f_{blade}

$$f_{\text{blade}} = N_b \cdot f_n, \quad (3.17)$$

where N_b is the number of blades and f_n is the shaft frequency from (3.3). Due to the **struts**, which are necessary for the stability of the fan, an interference noise can occur

$$f_{\text{interference}} = N_s \cdot f_{\text{blade}}, \quad (3.18)$$

where N_s is the number of struts. Another aerodynamic effect in the case of fans is the **“rotating stall”**. The rotating stall occurs based on flow separations in the individual but connected blade channels. Thus, a secondary flow occurs, which blocks a part of the channel. The relative speed of this blockade is almost 70 percent of the rotation speed in the opposite direction. Hence, this unsteady flow causes an acoustic noise, which can be estimated as [43, p. 93].

$$f_{\text{rot.stall}} \approx 0.7 \cdot f_{\text{blade}} \quad (3.19)$$

3.5.3 Electromagnetic excitation frequencies

The audible **electromagnetic** sound can be attributed to vibrations of some drive parts. These vibrations arise through magnetic forces, hence they are called “magnetic vibration” which can be generated by a permanent or induced source. The electromagnetic noise can dominate the hole sound power level, because it is situated in the most sensitive spectrum of the human ear [46]. The development of magnetic force over the mechanical system to the air-borne sound is shown in Figure 3.7.

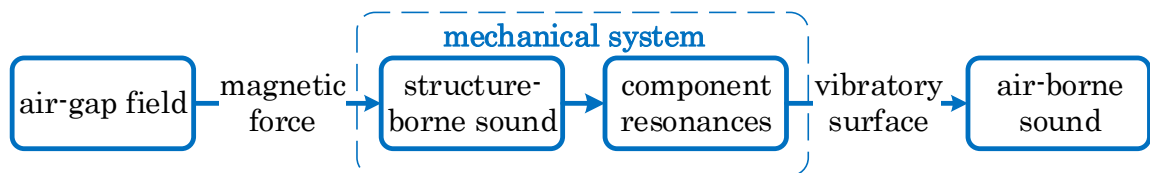


Figure 3.7: Magnetic sound development [34, p. 490].

Using the commutation frequency, the basic acoustic noise frequency of these torque ripples can be calculated as [38]:

$$f_i = i \cdot k \cdot p \cdot \frac{n}{60} \quad (3.20)$$

- i ... order of harmonics
- k ... number of steps in one electrical commutation loop
- p ... number of pole pairs
- n ... rotational speed in rpm

3.6 Common causes of noise and vibrations in electrical machines

The common causes of noise and vibration are presented in Table 3.1.

noise characteristic	cause	result
the vibration frequency has the first order	eccentric rotor, oval bearing ring	vibration
frequency and amplitude vary randomly	tight or deflected structure	air-borne sound, structure-borne sound, vibration
the vibration frequency has the first order or a multiply of it	friction	
high amplitude changes on low speed variation	resonance	
vibration amplitude changes during warming up the drive	thermal imbalance	
audible frequencies in the 200 to 500 Hz range	defect bearing	
whispering sound, broadband frequency spectrum	airflow	air-borne sound
the frequency is an integer multiple of the speed	siren effect	
the frequency is an integer multiple of the rotor slot number	siren effect of the internal airflow	

Table 3.1: Typical causes of noise and vibration [36, p. 269].

Chapter 4

Preliminary investigations

Several preliminary experiments have been carried out in the laboratory for familiarization with the quantities to be measured. Therefore, measurement and test setup equipment, which was available at the Electric Drives and Machines Institute, was used for the preliminary investigation. In addition, for the air-borne sound measurements in Chapter 4.1, a sound-insulating housing was placed on top of the setup to minimize the extraneous influence on the noise measurements.

4.1 Experimental setup: air-borne sound measurement

Figure 4.1 (a) shows the air-borne sound measuring setup. In order to measure the air-borne sound at the various positions, the fan system was suspended using elastomers. The used components are listed in Table 4.1. In Figure 4.1 (b) the measuring positions are indicated, which show the similarities to the array measurement. On the one hand this serves to determine the position of the highest sound level and, on the other hand, the respective frequencies (e.g., an increased turbulent inflow noise is expected at position 1). To separate the ambient noise from that of the fan system under test, an “empty measurement” was carried out before the actual measurement with the fan system deactivated.

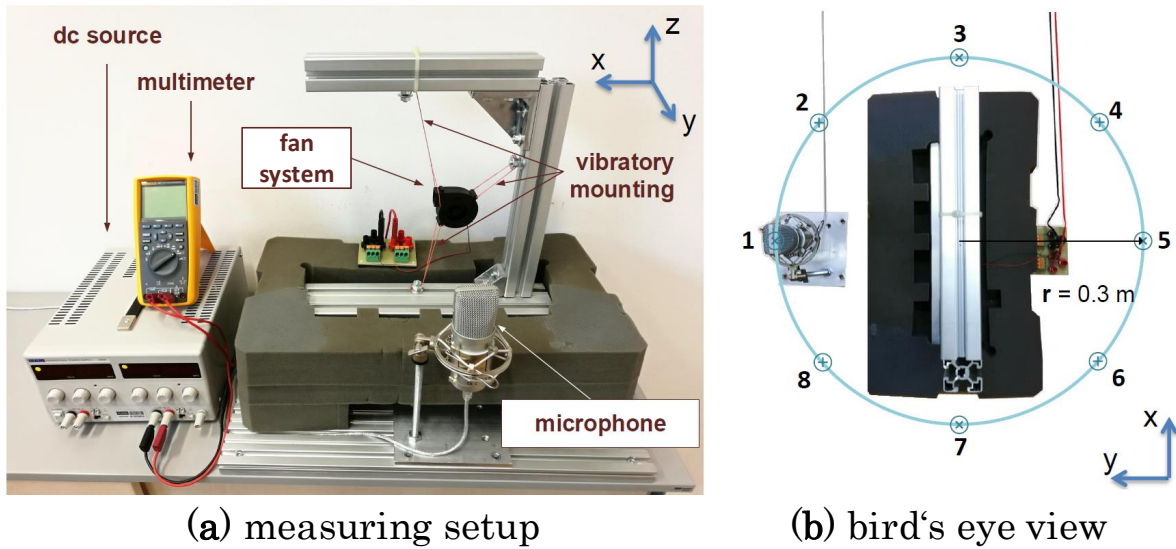


Figure 4.1: Microphone measuring setup (a) and positions (b).

component	designation
multimeter	Fluke 287 TRMS
DC-source	Aim-TTi EX354RD
Fansystem	E - I (see Table 4.3)
vibratory suspension	rubber bands
microphone	Auna MIC-900

Table 4.1: Used components of the measurement.

For the measurement, the fan drive was connected to the dc source, measuring the rms input current with a multimeter. The microphone was used to measure the noise of the fan system at the positions indicated in Figure 4.1 (b).

4.2 Experimental setup: structure-borne sound and current measurements

In addition to measurements with the microphone, current and vibration measurements have been performed to better allocate the frequencies that occur. Figure 4.2 shows the test setup and the components used for current and acceleration measurements. In addition, Table 4.2 lists all used components. To measure the vibrations, a triaxial accelerometer was used, which was attached to different positions on the housing with the help of rubber bands or double-sided adhesive tape. This acceleration sensor outputs an analog voltage proportional to the acceleration, which was recorded with a data recorder. For current measurement a current measuring box was used, which outputs a voltage proportional to the current. This voltage was also recorded with a data recorder.

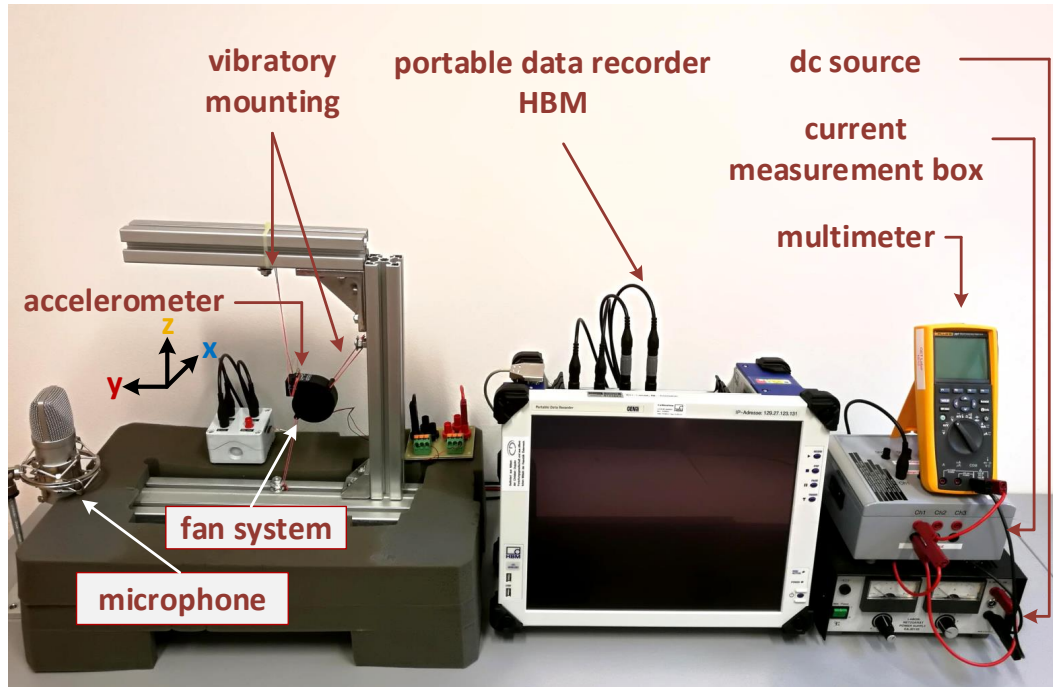


Figure 4.2: Acceleration and current measuring setup.

component	designation
multimeter	Fluke 287 TRMS
DC-source	Elektro-Automatik EA-3013 S
data recorder	HBM 1-GEN3i-2
three-axis accelerometer	ADXL 326
Fansystem	E - I (see Table 4.3)
current measurement box	EAM-CMB-1.5
vibratory suspension	rubber bands
microphone	Auna MIC-900

Table 4.2: Used components for the acceleration and current measurements.

4.3 Tested fan systems

Table 4.3 presents the characteristics of the studied axial (Fans A - D) and radial fan systems (Fans E - I).

Fansystem	voltage [V]	current [A]	speed [rpm]	blade quantity	type
A	12	0.2	2600	7	axial
B	12	0.24	2700	7	axial
C	12	0.21	4300	11	axial
D	12	0.13	2400	5	axial
E	8 - 16	0.135	5000	64	radial
F	9 - 16	-	5000	64	radial
G	9 - 16	-	4000	64	radial
H	9 - 16	-	6000	64	radial
I	8 - 16	-	5000	0	radial

Table 4.3: Fan systems under investigation.

Fansystems F to H have the same hardware as Fansystem E, but differ with re-

spect to the switching strategy. Fansystems F to H are implemented with an angle modulated switching strategy (AMSS), which needs only one switching cycle of the corresponding switch per electrical period, reducing the switching frequency and thus the electromagnetic emissions [25, p. 3].

Fansystem I is the same as Fansystem E but with the blades removed to minimize the aerodynamic noise. Figures 4.3 (a) and (b) illustrate a typical radial fansystem and its rotor (Fansystems E - H). The rotor of Fansystem I is depicted in Figures 4.3 (c).

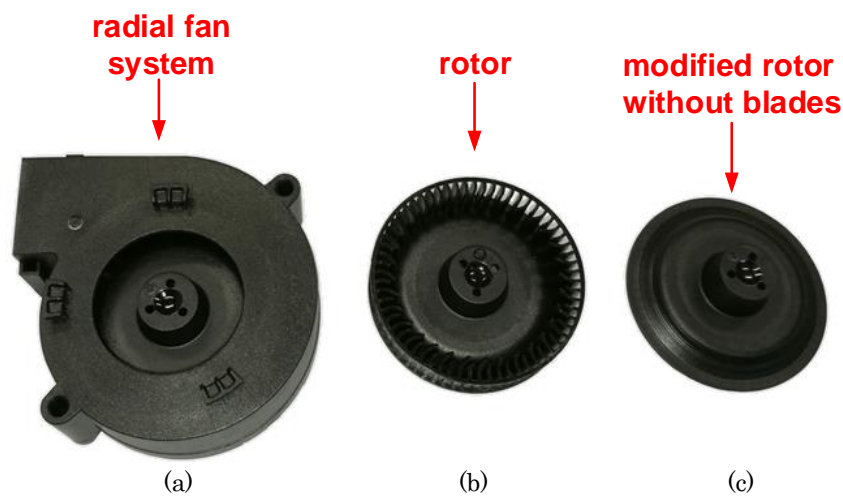


Figure 4.3: Typical radial fan rotor and modified rotor.

4.4 Stator excitation investigations

In order to estimate how strongly magnetostriction and the potential movement of the coils affect the entire noise spectrum, two stators without a rotor were energized with different frequencies by using a function generator. The noise emitted by the stators was measured with a microphone and then evaluated with Matlab. Figure 4.4 shows the simplified testing setup where a function generator (RS PRO, type AFG-21112) was used for the source. The stators to be tested with installed windings were removed from the Fansystems B and E, see Table 4.3.

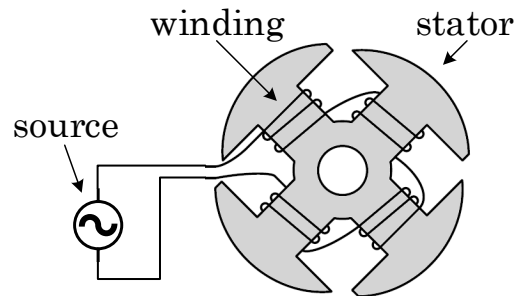


Figure 4.4: Schematic experimental setup for the stator excitation investigations.

On the one hand, double the supplied frequency was expected due to the magnetostriction, see Chapter 3.3. On the other hand, a “breathing” of the coil (similar to a mode 0, which is described in [35, p. 64]) is expected. The Fansystems B and E in Table 4.3 were dismantled and their stators were measured. The setup shown in Figure 4.1 was used with the exception of the power supply, which was replaced by the function generator type AFG-21112. The applied frequency was increased from 50 Hz to 40 kHz as sinusoidal, rectangular, and triangular signals, whereby the voltage amplitude was set such that the maximum permissible coil current was not exceeded. With Fansystem E neither a noise was audible or measurable. With Fansystem B, a very low noise could be perceived and measured, which is probably due to the fact that the windings have loosened over time. In conclusion, it was found that magnetostriction and coil deformation play a minor role in the overall noise development.

This experiment was additionally carried out with the rotor at rest ($n = 0$), whereby the emitted noise differs significantly from the previous experiment because the magnetic field of the stator interacts with the magnetic field of the rotor. On the one hand, this is due to the fact that the rotor forms a vibratory surface and, on the other hand, the magnetic field generated by the permanent magnet attracts and repels the one generated by the energized stator windings resulting in rotor oscillations.

4.5 Current measurements

Electromagnetic noise is essentially caused by forces in the air-gap which can develop vibrations depending on the transfer function of the mechanical system, as described in Chapter 3. Energizing the motor coils, a magnetic field is generated leading to magnetic forces. Measuring and subsequently evaluating this current, these forces and their frequencies can be estimated.

Notice that the current which produces the force is that through the coils, see the current i_p in Figure 1.11. Frequently, measuring this current is a challenging task which merely can be realized by modifications of the application. It is easier to measure the supply current i_{DC} .

To determine the difference between these two options (and whether it is sufficient to measure the supply current only), both the coil and supply currents of a modified radial fan system were measured and evaluated. Figure 4.5 (a) illustrates the coil currents of sub-phase 1 and 2 for one electrical revolution on the left. On the right, the respective order analyses are presented. The left hand side, Figure 4.5 (b) shows a comparison of the supply current i_{DC} and the sum of absolute values of the coil currents i_{coil1} and i_{coil2} . On the right, the respective order analyses are illustrated. In consequence of the small deviations, an evaluation on the basis of the supply current is sufficient.

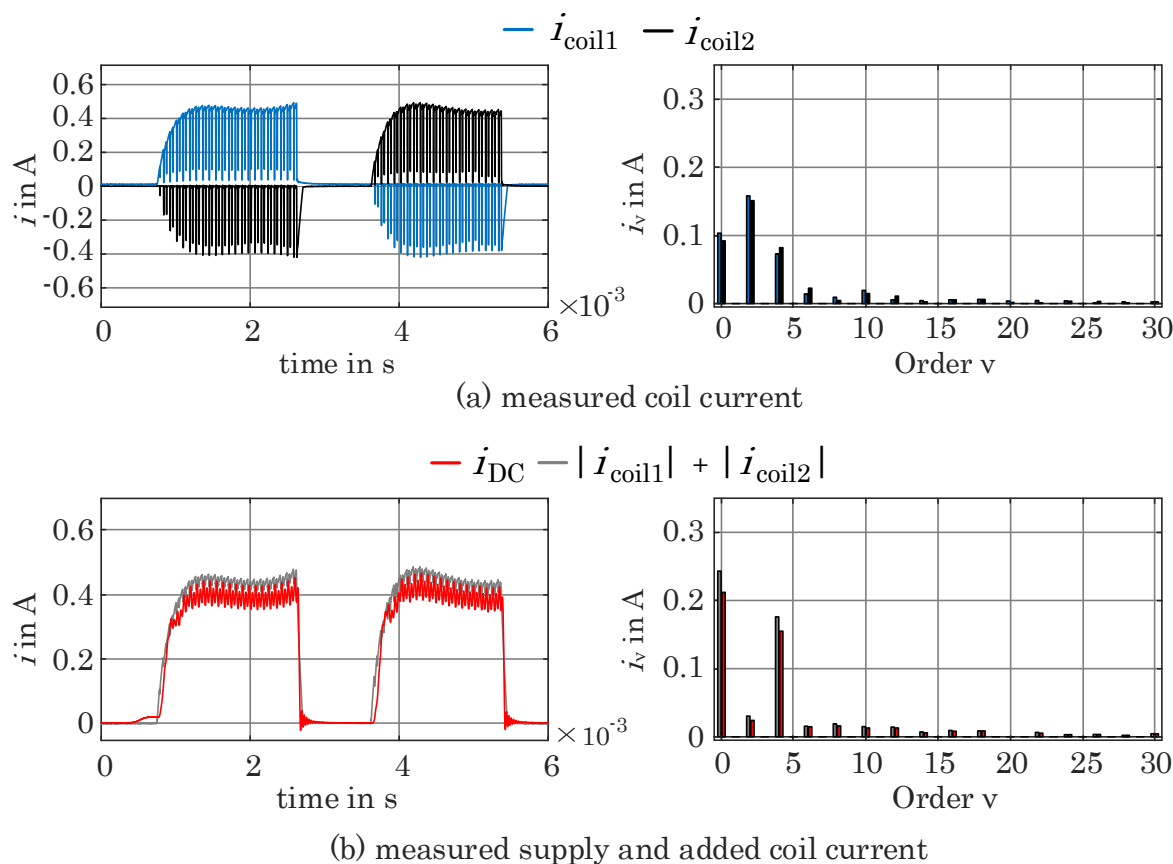


Figure 4.5: Measured coil currents in (a) and supply and added coil currents in (b) of the Fansystem E. The order analyses are illustrated on the right.

In addition, another switching strategy with the same hardware has been investigated. This angle modulated switching strategy (AMSS) generates one current block per electrical period, which reduces the switching frequency and thus the electromagnetic emissions [25, p. 3]. As the shape of the currents change, the electromagnetically produced forces and thus the noise will also change. Figure 4.6 shows the current curve on the left and its order analysis on the right.

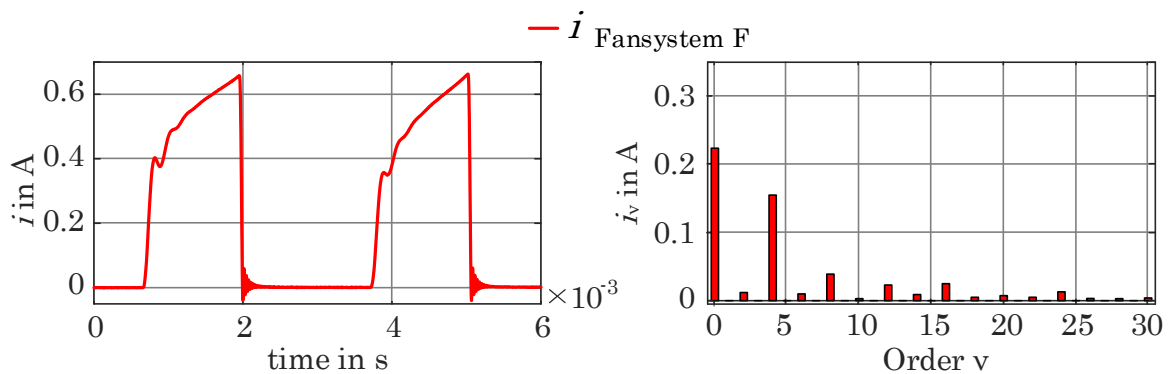


Figure 4.6: Measured supply current and its order analysis of the Fansystem F operated with AMSS.

In order to separate the aerodynamic noise from the electromagnetic noise, radial fan system without blades was fabricated (Fansystem I). Due to the reduction in air resistance and weight the current is expected to be smaller. (A test showed that a weight adjustment of the rotor did not yield better results.) However, the rotating speed remains unchanged as the drive speed is controlled. Figure 4.7 shows the measured current of Fansystem I on the left and its order analysis on the right.

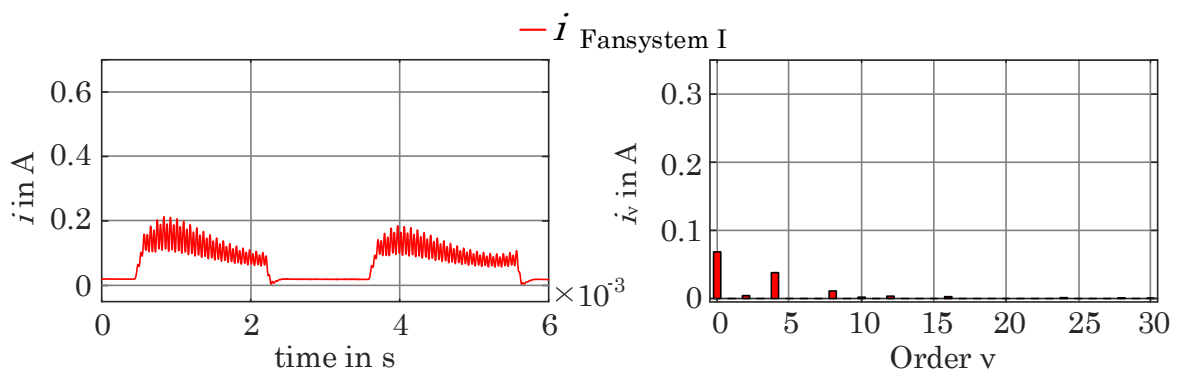


Figure 4.7: Measured current of Fansystem I and its order analysis.

To ensure a comparable evaluation of the fans system with and without blades (Fansystems E and I), their current shapes and order analyses have to be similar. Figure 4.8 illustrates a comparison between Fansystem E and I. As can be seen, the waveforms are similar (block shape) as are the significant peaks in the order analysis, which makes an evaluation possible.

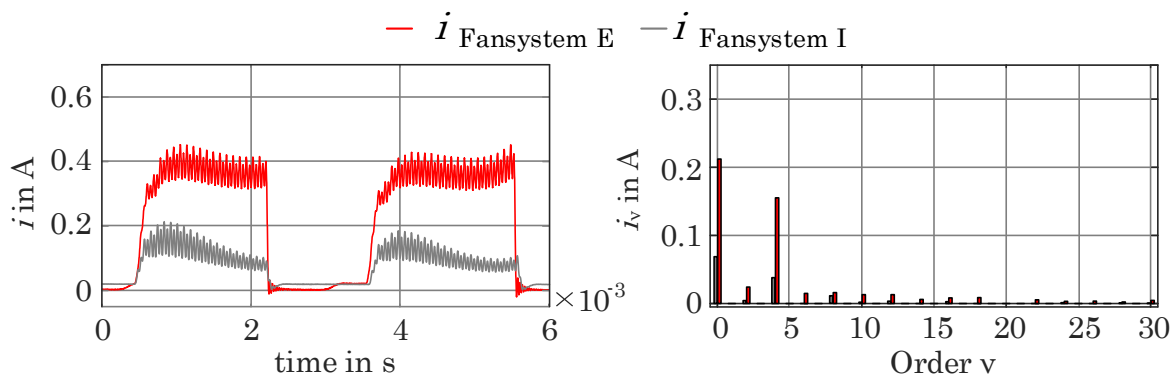


Figure 4.8: Comparison of the measured currents and order analysis of Fansystems E and I.

4.6 Comparison: measured versus approximated current waveforms

Varying current waveforms can be found in sub-fractional horsepower motors. Knowing the approximate current shape (e.g., calculated by finite element method or through experience), occurring harmonic components (i.e., frequencies) can be estimated. The following figures contrast three typical current waveforms (observed during the measurements) and their rough analytic approximation as well as the respective order analyses.

On the left, Figure 4.9 shows the supply current of the radial Fansystem E from Table 5.3 and its rough analytic approximation. On the right, an order analysis of both curves is shown.

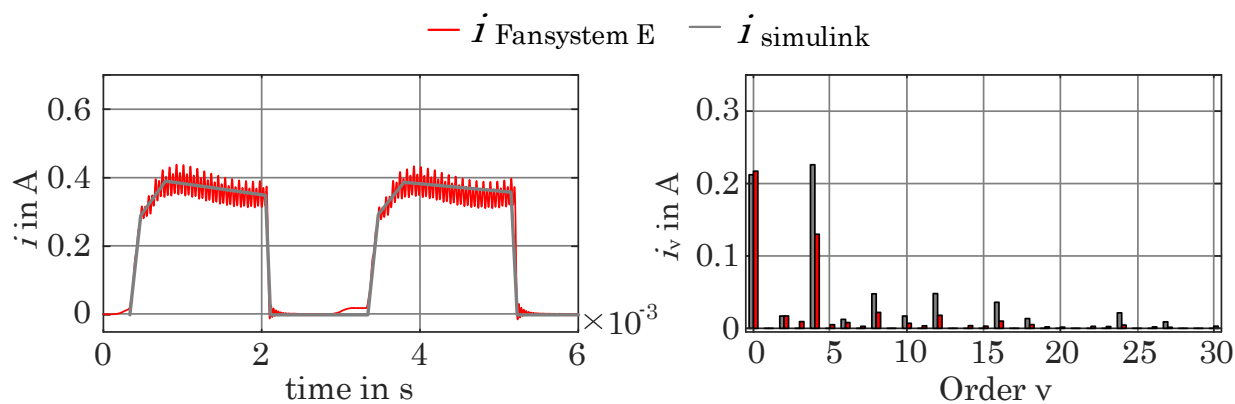


Figure 4.9: Comparison of simulated and measured currents of Fansystem E.

On the left, Figure 4.10 shows the supply current of the radial Fansystem F from Table 4.3 which uses the AMSS switching method and its rough approximation. On the right, an order analysis of both curves is shown.

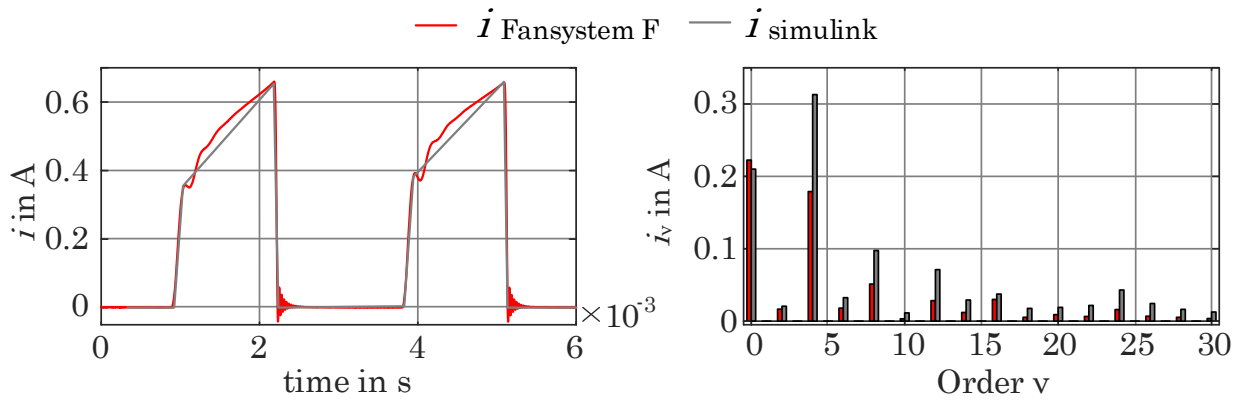


Figure 4.10: Comparison of simulated and measured currents of Fansystem F.

On the left, Figure 4.11 shows the supply current of the modified radial Fansystem I from Table 5.3 which has no blades and its rough analytic approximation. On the right, an order analysis of both curves is shown.

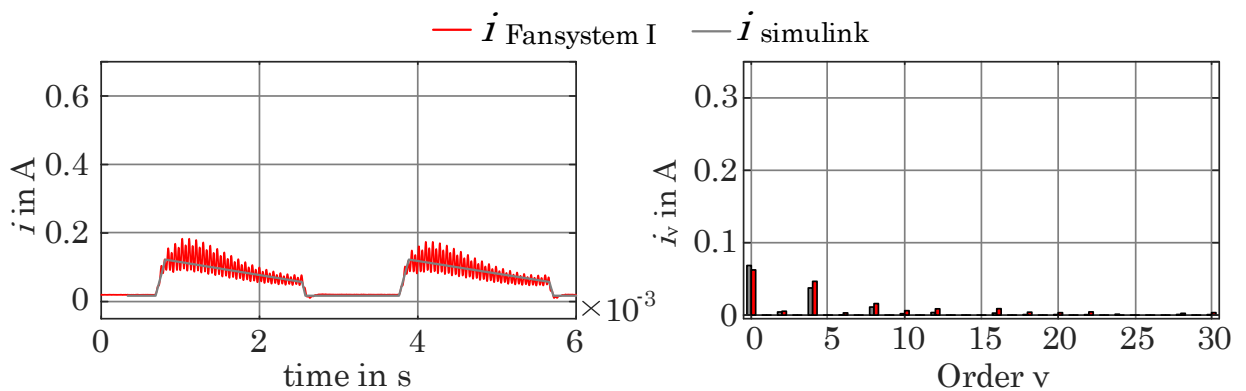


Figure 4.11: Comparison of simulated and measured currents of Fansystem I.

As can be seen in Figures 4.9-4.11, having knowledge of the approximate current shape, the occurring frequencies of the order analysis can be determined. The general characteristic remains, only the amplitudes vary. Also, a variation of the duty cycle (i.e., the length of the current block) changes the amplitudes, but not the occurring frequencies. Finally, these harmonics can trigger resonances of the system and lead to noise.

4.7 Influence of rotor imbalance

A rotor imbalance usually manifests itself in a first order component in the noise spectrum equal to the rotational frequency [36]. For validation, a simple experiment was implemented. On Fansystem A (see Table 4.3), different masses were fixed on the positions 1 and 2 in Figure 4.12 to produce an imbalance.

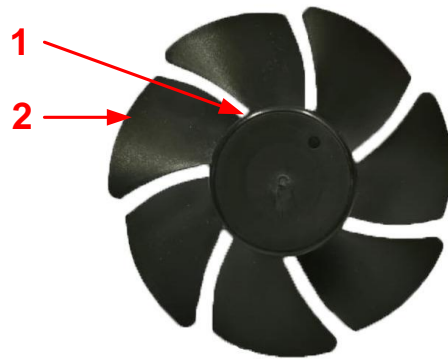


Figure 4.12: Positions of additional masses for imbalance investigations.

The following scenarios have been implemented:

- a mass of 0.7 g was fixed at the inner radius (see position 1)
- a mass of 0.7 g was fixed at the outer radius (see position 2)
- a mass of 1.05 g was fixed at the outer radius (see position 2)

The measurements have been performed with an accelerometer and a microphone (see Figures 4.1 and 4.2). The significant increase of the first order could be determined with both measuring methods, the acceleration sensor and the microphone. The increase of the first order component determined by measuring the air-borne sound with a microphone is illustrated in Figure 4.13. A measurement without unbalance was carried out for reference (i.e., 1 pu). The measured increase of the first order component is significant and amounts to more than 300%, 1600% and 2350% respectively, see Figure 4.13.

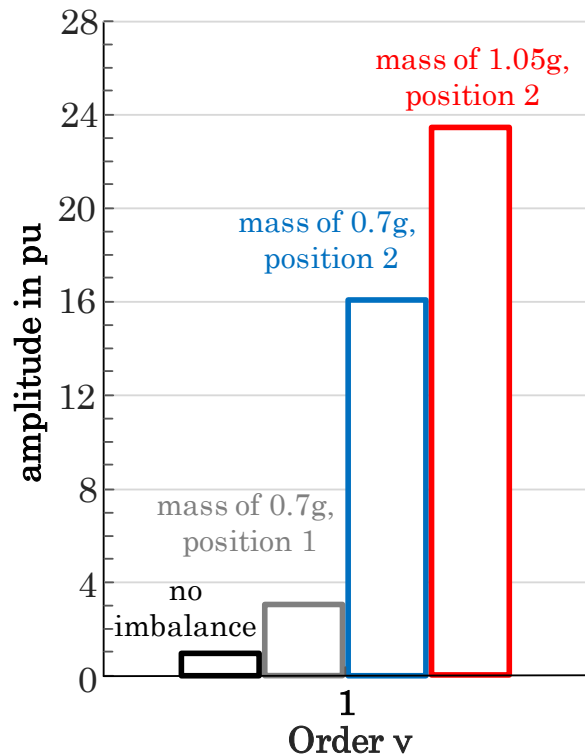


Figure 4.13: Change in the first order compared of Fansystem A for different imbalances measured with an acceleration sensor.

4.8 Investigations of blade passing noise (BPN)

The blade passing noise is a common property of axial fans, which often dominates the generated noise. This BPN can be calculated as the product of revolutions per second, the number of blades, and integer multiples thereof (see Chapter 3.5.2). For validation, measurements on four different fan systems (see Fansystem A-D in Table 4.3) were performed. Exemplary, Figure 4.14 shows the peaks of the blade passing noise of Fansystem C. This fan system has a speed of 4300 rpm and hence a rotational frequency of 71.66 Hz, which poses the first order (3.3). Using (3.17) and the number of fan blades, the blade passing frequency yield an 11th order. This can also be seen in Figure 4.14. In addition, multiples of the blade passing frequency can also be observed. The shown peak distribution is characteristic for axial fans and the measurement results are repeatable. Also the other axial fans (see Fansystems B-D in Table 4.3) showed the described characteristics.

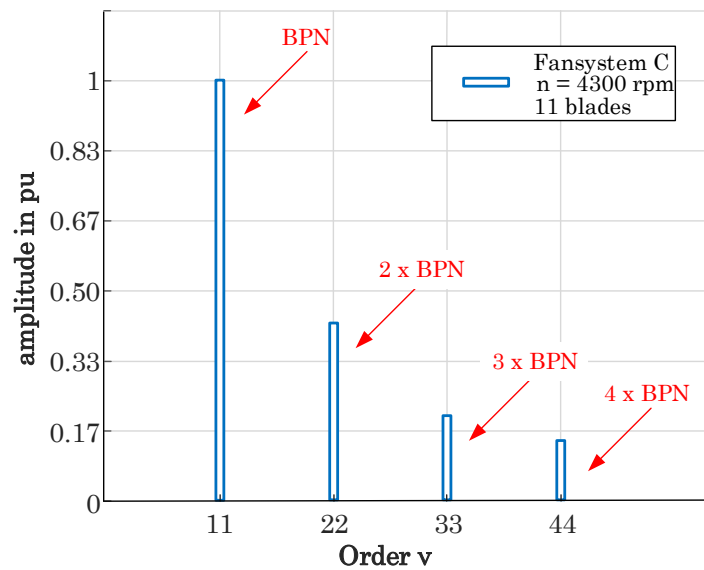


Figure 4.14: Example of blade passing noise of Fansystem C

Conversely radial fans usually show a broadband noise instead of significant peaks since the number of blades is significantly higher leading to turbulences.

4.9 Comparison: acceleration, current, and microphone measurements

To allocate the observed frequencies to the individual noise sources (see Figure 3.1), the measured current, the vibrations measured with a triaxial accelerometer, and the microphone signal are compared (see Figure 4.15). The accelerometer was mounted as shown in Figure 4.2, although it should be noted that this position was not optimal. When a certain frequency is only present in the microphone signal, it is most likely caused by an aerodynamic source. If a frequency occurs in the signal of the acceleration sensor or the current measurement as well, electromagnetic or mechanical sources may have caused this noise component. For illustration, an order analysis (i.e., the normalization to the rotational frequency), is chosen to simplify the evaluation.

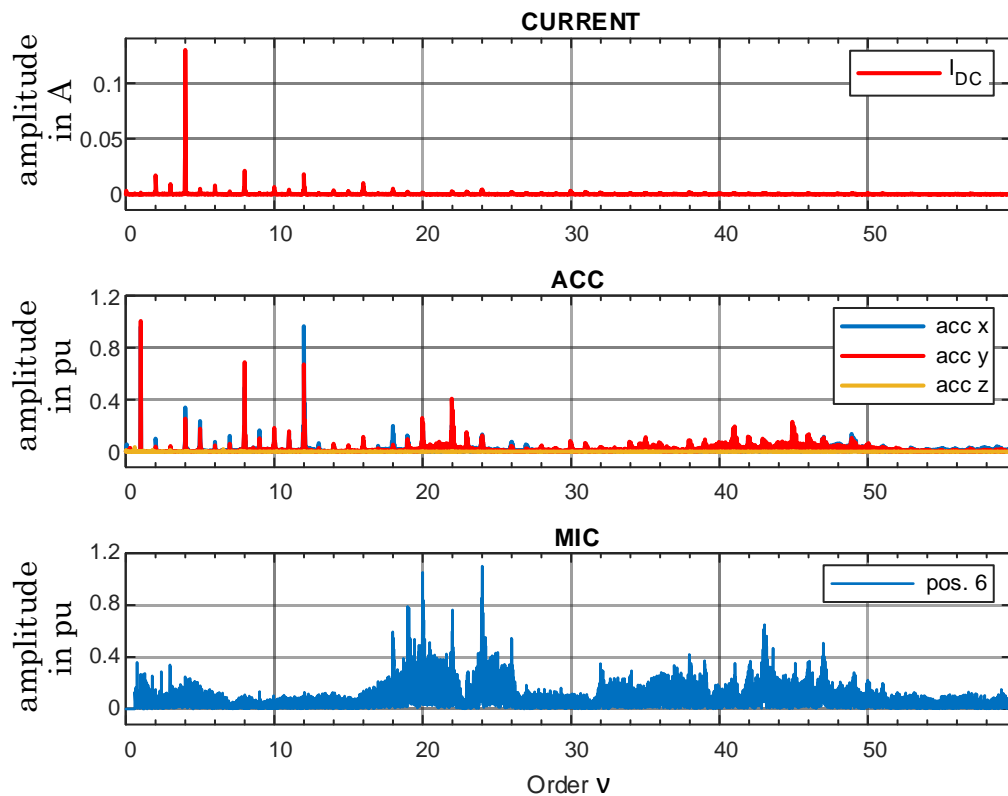


Figure 4.15: Comparison of the occurring frequencies of the supply current, acceleration sensor, and microphone of position 6 (see Figure 4.1 (b)) measurements.

A first order component, which indicates a mechanical imbalance, is clearly visible in both the accelerometer and the microphone measurement results (this is discussed in Chapter 4.8). The fourth order is highly pronounced in the current measurements, which can be explained by the four current pulses per revolution in a single-phase four-pole machine. This fourth order is also visible in the accelerometer, as well as in the microphone measurements and can hence be assigned to the electromagnetic source. The current also has distinct higher harmonic such as the 8th, 12th, and 16th order components which may be the reason for the same in the acceleration measurements, as they can excite natural frequencies of the mechanical system and housing. However, the higher order components in the acceleration and microphone measurements are not due to the current. In fact, the distinct noise components in the microphone measurements are of higher order and most likely due to aerodynamic noise sources. As they are partly reflected in the signal of the acceleration sensor, they may be due to oscillations of the housing.

Remark: The cut-off frequency of the used acceleration sensor is 500 Hz which is about the sixth order. Therefore, the results beyond the sixth order must be considered with caution. Measurements with more precise acceleration sensors are described in Chapter 5.2.

Figure 4.16, which compares three fan systems from Table 4.3, offers a further comparison. Shown in blue is the order analyses of the radial Fansystem E, which has 64 blades. Furthermore, there are two versions of the Fansystem I, which is identical to Fansystem E in terms of construction, but has no blades: The balanced radial fan system I which is shown in yellow was balanced after removing the fan blades and the unbalanced version which is shown in red was balanced before.

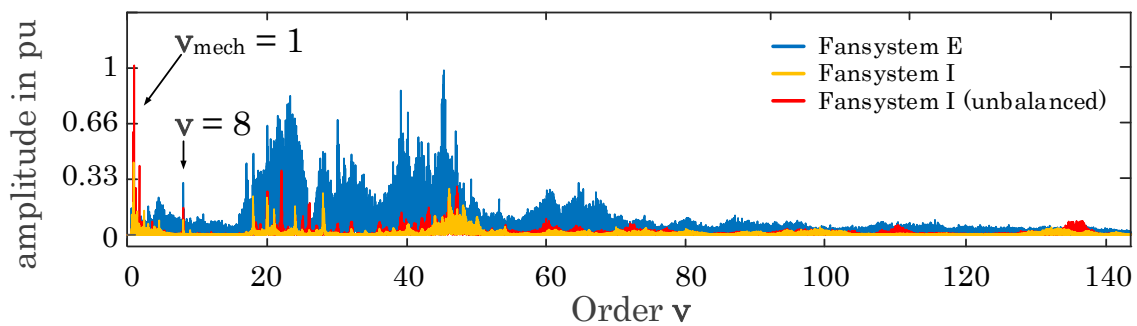


Figure 4.16: Comparison of the occurring frequencies of the microphone measurement at position 2 (see Figure 4.1 (b)) of three different fan systems from Table 4.3.

As expected, the first order component of the unbalanced version of Fansystem I is strongly pronounced. (The increase of the first order with increasing unbalance can be observed in all rotating machines and is discussed in Chapter 4.7.) The eighth order is also pronounced, which might be excited by the 8th order of the current. Comparing Fansystem E and I shows that the aerodynamic noise was greatly reduced in the whole frequency spectrum due to the removal of the blades in Fansystem I. The measurement of Fansystem I which has no blades also reveals an increase in the range of order 135 to 140, which about half the PWM frequency. This accumulation can also be observed in the more sophisticated measurements in the audio laboratory (see Chapter 5.1) and can be explained by the use of frequency hopping PWM in which the switching frequency alternates between two selected switching frequencies every switching cycle.

Chapter 5

Measurements in a low reflection chamber

In order to yield reproducible and high quality air-borne and structure-borne sound measurements, the experiments presented in this chapter have been carried out in a low-reflection chamber at the Electronic Music and Acoustic Institute (University of Music and Performing Arts, Austria) using precision measuring instruments, see Figure 5.1. First, the experimental test setups for the air-borne and structure-borne noise measurements are described, as are the fan systems under investigation. Then, the data processing and signal conditioning are elaborated upon. Finally, the measurement results are presented and discussed.

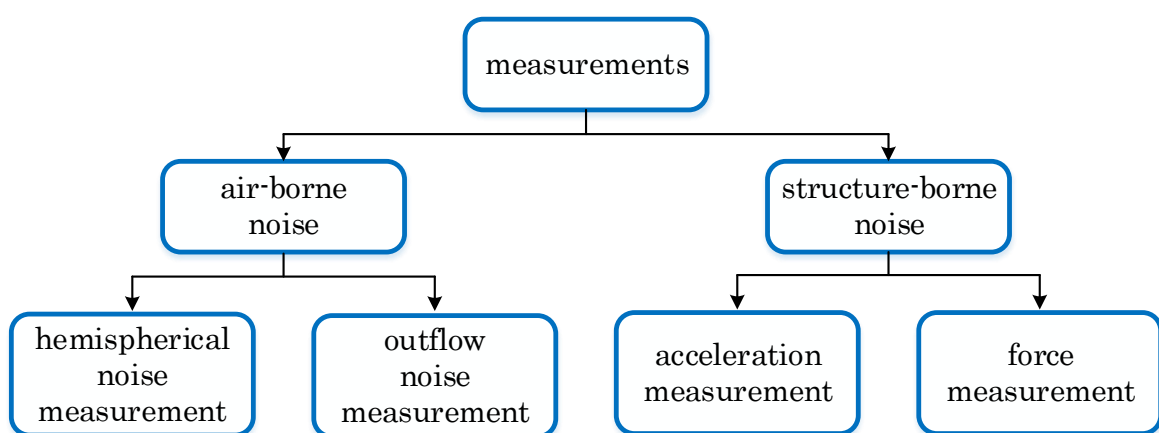


Figure 5.1: Overview of the performed measurements.

5.1 Experimental setup: air-borne sound measurements

The air-borne sound measurements have been carried out using microphones according to the international standard ISO 13347-3 [48] as far as possible. A type A test setup (free inlet, free outlet) was realized. In addition, the noise difference is more than 10 dB from the component level to be measured, since the measurements are carried out in a low-reflection room. The used microphones have been calibrated with an acoustic calibrator prior to the measurements. The calibration and evaluation processes are described in detail in Chapter 5.5.2. The components used for the air-borne sound measurements are listed in Table 5.3.

component	designation
multimeter	Fluke 287 TRMS
DC-source	12 V Battery
Microphone amplifier	ANDIAMO.MC
Acoustic calibrator	Type 4231
vibratory suspension	rubber bands
microphone	NTI M2230
reference microphone	Earthworks M55
reference measuring equipment	Norsonic Nor140
Fansystems	see Table 5.3

Table 5.1: Used components for the air-borne sound measurements.

5.1.1 Hemispherical measurement setup

Figures 5.2 and 5.3 (a) exhibit the setups for the near- and far-field measurement using microphone arrays. The respective microphone positions are indicated in Figure 5.3 (b). For the near-field measurements a radius of 0.3 m was selected to easily compare the results with those obtained from the preliminary investigation in Chapter 4. For the far-field measurements, the spherical microphone array in Figure 5.2 was used which was available at the acoustic laboratory coming with a radius of 1.2 m.

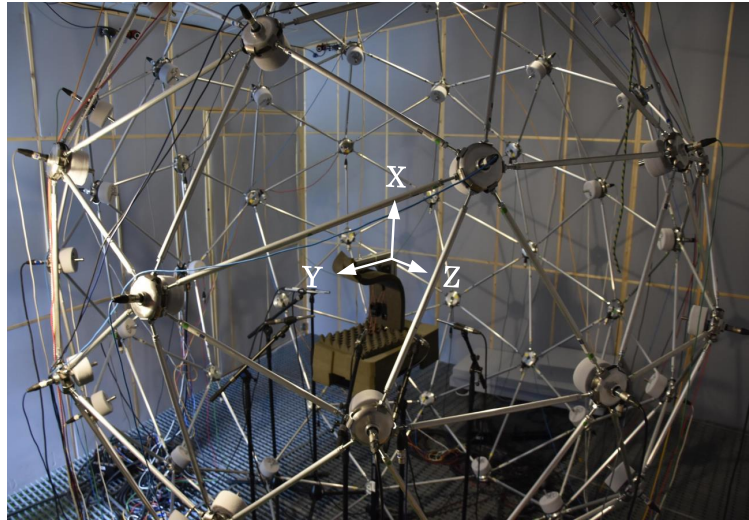
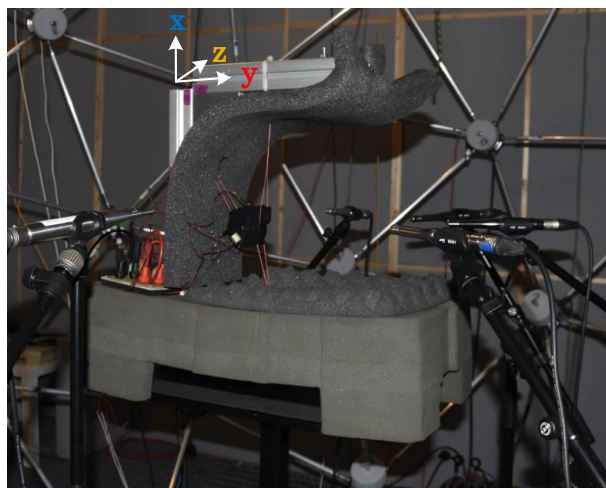
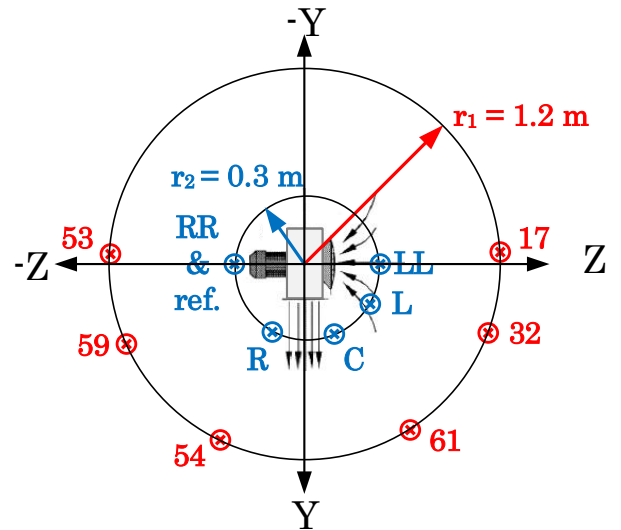


Figure 5.2: Test setup for the near and far-field measurements using microphone arrays.



(a) near-field air-borne sound measurement setup



(b) bird's eye view

Figure 5.3: Closeup showing the near-field measurement setup (a) and microphone positions for the near- and far-field array measurements (b).

5.1.2 In- and outflow noise separation measurement setup

Aiming to distinguish the inflow from the outflow noise, the test setup shown in Figure 5.3 was modified using a separating element as illustrated in Figure 5.4. This test was carried out in approximation of the hall room method, which is described in the German standard DIN 45 635 Part 38 [49]. Only the ventilation opening to be measured should be guided through a low-vibration, closed channel into the hall room, see Figure 5.4 (a).

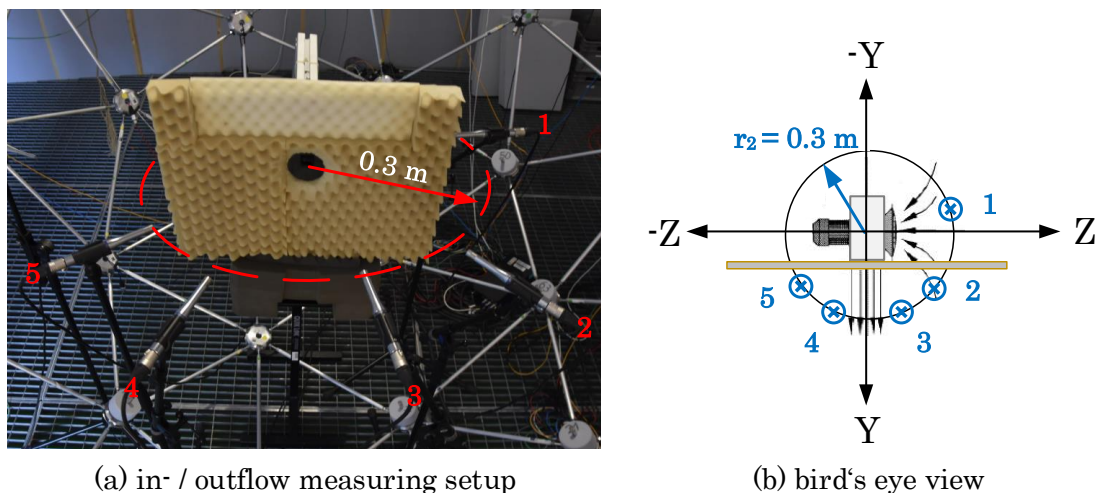


Figure 5.4: Measurement setup (a) and the positions of the microphones (b).

As can be seen in Figures 5.4 (a) and (b), a plate separates microphone 1 from the other microphones. Hence, the microphones 2 to 5 are expected to record primarily the outflow noise, as the inflow noise is expected to be significantly reduced. Conversely, it is expected that microphone 1 will record primarily the inflow noise due to the separating element.

5.2 Experimental setup: structure-borne sound measurements

The structure-borne sound measurements have been carried out using three single-axis acceleration sensors mounted on the housing of the tested fan systems and two force sensors where the fan systems are mounted onto a stainless steel cylinder using screws. The components used for the measurements are listed in Table 5.2.

component	designation
multimeter	Fluke 287 TRMS
DC-source	12 V Battery
vibratory suspension	rubber bands
amplifier	Nexus conditioning amplifier type 2690
3 single-axis acceleration sensor	Brüel & Kjaer ISOTRON 2250AM1-10
force sensor	PCB M260A01
Fansystems	see Table 5.3

Table 5.2: Used components for the structure-borne sound measurement.

5.2.1 Acceleration sensor measurement setup

For the acceleration measurement, the fan system is suspended at three points using rubber bands, like in the noise measurements (see Figure 5.5). Three single-axis accelerometers are mounted at defined positions on the fan housing in the x -, y -, and z -directions using a mounting wax. (Advantageous to this setup is the concurrent measurement of air-borne and structure-borne noise.) For evaluation, the acceleration signal in g must first be multiplied by 9.81 (to obtain a result in m/s^2) and subsequently by the fan system's mass (to obtain a result in N), see Chapter 5.5.1.



Figure 5.5: Measurement setup for the acceleration measurements.

As discussed in Chapter 1.7, the total mass of the sensors applied should not exceed approximately 10% of the mass of the device under test [29, p. 12]. Due to the low mass of the used sensors (0.4 g per piece), the total sensor mass amounts to around 5 percent of the fansystem's mass, which is acceptable.

5.2.2 Force sensor measurement setup

For the force measurement, the fan system is directly screwed to the force sensors (see Table 5.2) with 0.8 Nm at two points, see Figure 5.6. The force sensors are attached to a stainless steel cylinder, which is uncoupled from the bottom support.

Since the mass of the cylinder is very high compared to the mass of the fan system, the steel cylinder can be denoted as a rigid abutment as described in the industrial standard [50, p.8].

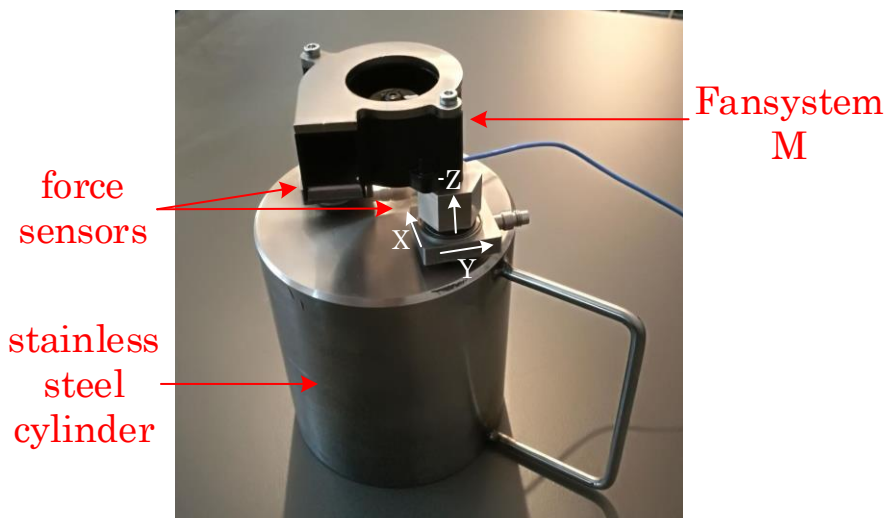


Figure 5.6: Measurement setup for the force measurements.

Each measurement has been performed twice, because the pre-amplifier offers only four inputs and therefore each sensor is read separately. The data processing and signal conditioning is similar to that described in Chapter 5.5.1. Merely, the product-specific sensitivity of the sensor (2.25 mV/N) must be set in the pre-amplifier. Furthermore, the acceleration constant g and the fan system's mass m are omitted in (5.2), since this force sensor directly generates a voltage which is proportional to the force in Newton.

5.3 Experimental setup: standardized measurements

In order to bring a product onto the market, it is necessary that it complies with certain standards. As already discussed in Chapter 1.1, the noise standards for automotive auxiliary drives are still being developed and will become increasingly important in the coming years. Companies often have in-house standards which may have stricter requirements the product has to meet. An example is, the Volkswagen standard (VW 82469) [50], which describes the acoustic demands of auxiliary equipment. This standard was selected to perform standardized measurements, see Chapter 5.6.4. It requires both air-borne and structure-borne sound measurements for auxiliary drives such as window lifts, control motors, relays, pumps, and fan systems. One-third-octave band analyses have to be carried out, which should not exceed the provided limits.

The measurement setup for **air-born** sound measurements is based on the DIN EN 61672-1 standard. To comply with this standard, the sound power of the loudest point at a defined is to be evaluated. The A-rated one-third-octave spectrum should not exceed the provided limits and the total sound pressure level has a limit as well. In order to ensure that the loudest point is measured, two microphones have been placed at distances of 0.5 m and 1.0 m in both the inflow and outflow directions, see Figure 5.7.

Remark: It is very important to use a microphone windshield and to avoid direct wind blowing. Otherwise, the measurements will be influenced significantly.

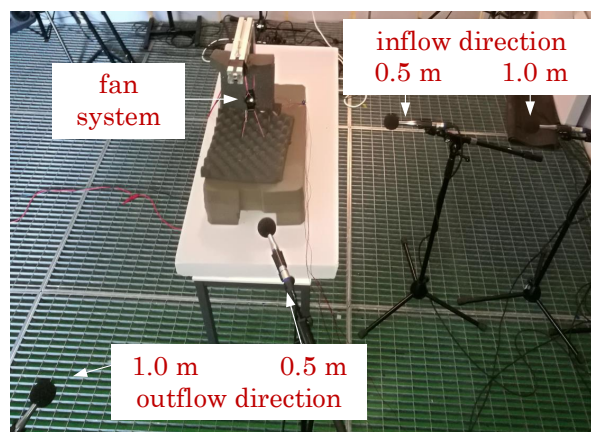


Figure 5.7: Measurement setup for the standardized measurement.

For the **structure-borne** sound measurements, three acceleration sensors have been mounted directly on to the fan system as described in Chapter 5.2.1. Another possibility is the use of force sensors, which must be measured in a separate setup. Basically, the forces in the attachment points are required in the industry standard [50, p.9].

5.4 Fan systems under investigation

Table 5.3 presents the radial fan systems, which were used for the air-borne and structure-borne noise measurements.

Fansystem	voltage [V]	current [A]	speed [rpm]	blade quantity	type
E	8 - 16	0.135	5000	64	radial
F	9 - 16	-	5000	64	radial
G	9 - 16	-	4000	64	radial
H	9 - 16	-	6000	64	radial
I	8 - 16	-	5000	0	radial
J	14	0.3	7000	37	radial
K	14	0.3	6850	37	radial
L	14	0.3	6650	37	radial
M	14	-	-	-	radial
N	14	-	-	37	radial

Table 5.3: Fan systems under investigation.

5.5 Data processing and signal conditioning

The data processing and correct signal conditioning are important aspects of the noise evaluation. Using calibration signals, the measured signals must be scaled to obtain correct results. The following subsections describe the data processing and signal conditioning of the accelerometer and microphone measurements.

5.5.1 Accelerometer measurements

Figure 5.8 shows the signal conditioning for the accelerometer measurements.

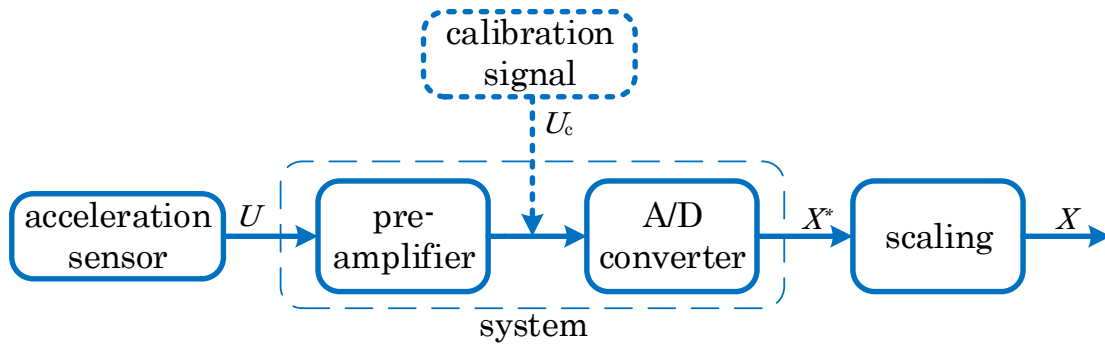


Figure 5.8: Block diagram for scaling of the accelerometer signal.

The used acceleration sensor has a product specific sensitivity (e.g., 10 mV/g) which needs to be set in the pre-amplifier. Furthermore, this pre-amplifier offers the opportunity to select a proper signal amplification to make full use of the input range of the used A/D converter. The selected output sensitivity of the pre-amplifier $x_{\text{sen}} = 316 \text{ mV/g}$.

The used accelerometer measuring system offers a build-in calibration process, in which a sinusoidal calibration signal U_c with an rms value of 1 V and a frequency of 1 kHz is applied to each channel of the A/D converter and can be recorded for reference. The rms value of the obtained signal X^* , is denoted as $k_{c,\text{acc}}$, which is essentially the attenuation factor of the A/D converter.

The scaling factor can then be calculated using the output sensitivity of the pre-amplifier x_{sen} and the obtained attenuation factor $k_{c,\text{acc}}$:

$$c_{\text{acc}} = \frac{1}{k_{c,\text{acc}} \cdot x_{\text{sen}}} \quad (5.1)$$

This scaling factor is valid for the linear region of the accelerometer's frequency characteristic.

To obtain the signal X in Newton the system's output signal X^* must be multiplied by the scaling factor c_{acc} , the mass of the object m (i.e., fan system), and the gravitational constant g .

$$X = X^* \cdot c_{\text{acc}} \cdot m \cdot 9.81 \frac{\text{m}}{\text{s}^2} \quad (5.2)$$

The scaled signal X can then be processed further. For additional evaluation, an order analysis and a one-third-octave band analysis can be performed, the latter, e.g., with the Matlab function “p octave”.

c_{acc}	...	scaling factor
$k_{c,acc}$...	attenuation factor of the A/D converter
x_{sen}	...	sensitivity factor in mV/g
m	...	mass of the fan system in kg
X^*	...	system output
X	...	scaled signal in N

To create a one-third-octave band using the “p octave” function, the input signal $X_{poc,in}$ is the time-dependent force signal X divided by a reference force F_0 :

$$X_{poc,in} = \frac{X}{F_0} = \frac{X}{1N} \quad (5.3)$$

Then the square root of the “p octave” output signal $X_{poc,out}$ multiplied with the reference signal F_0 must be taken and multiplied by the reference force to obtain the force one-third-octave spectrum, see (5.4).

$$F_{third} = \sqrt{X_{poc,out}} \cdot F_0 \quad (5.4)$$

If the sum of forces is to be determined, this must be done with the addition of power values and then be multiplied with the reference signal F_0 , see [50, p.9]. To be more specific, see (5.5).

$$F_{third,sum} = \sqrt{X_{poc,out,1} + X_{poc,out,2} + \dots + X_{poc,out,n}} \cdot F_0 \quad (5.5)$$

$X_{poc,in}$...	conditioned p octave input signal
$X_{poc,out}$...	p octave output signal
F_0	...	reference force of 1 N
F_{third}	...	force one-third-octave spectrum in N
$F_{third,sum}$...	Total force one-third-octave spectrum in N

For illustration, Figure 5.9 shows step by step what the function “p octave” outputs and how the data is processed.

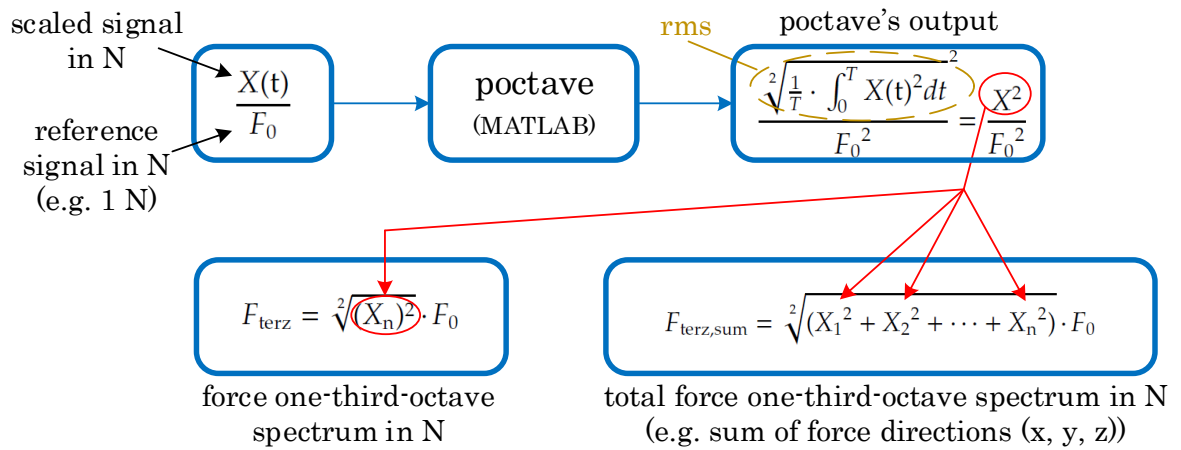


Figure 5.9: Stepwise illustration of “p octaves” output and the data processing for the force measurements.

5.5.2 Microphone measurements

Figure 5.10 illustrates the data processing and conditioning for the microphone measurements. For reference, a calibration signal U_c with a sound pressure level of 94 dB, corresponding to 1 Pa, at a frequency of 1 kHz is applied to each microphone and recorded for reference. U represents the noise of the object to be measured. The unscaled output signal of the system is referred to as X^* .

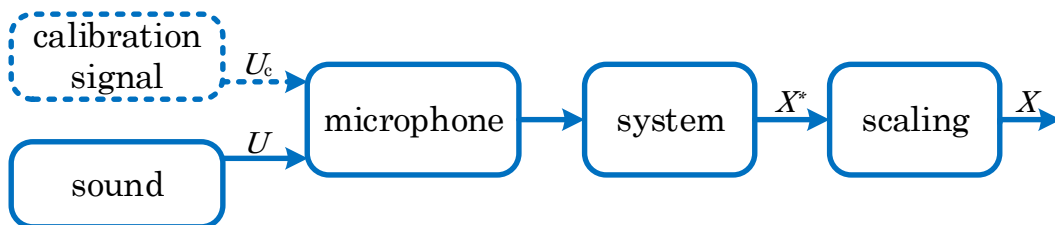


Figure 5.10: Block diagram for scaling of the microphone signal.

The amplitude $p_{c,mic}$ obtained from the calibration signal at the frequency of 1 kHz can easily be evaluated using an FFT. The scaling factor c_{micro} can then be calculated as:

$$c_{micro} = \frac{\sqrt{2}}{p_{c,mic}} \quad (5.6)$$

This scaling factor is valid for the linear region of the microphone's frequency characteristics.

Next, the system's output signal X^* must be multiplied by the scaling factor c_{micro} to obtain the scaled signal, see (5.7).

$$X = X^* \cdot c_{micro} \quad (5.7)$$

c_{micro}	...	scaling factor
$p_{c,micro}$...	peak value of the calibration signal
X^*	...	system output in Pa
X	...	scaled signal in Pa

Remark: It is very important that the calibration signal has the same length as the signal of interest.

For evaluation, an FFT and subsequently a one-third-octave band analysis can be performed. Equation (5.8) is used to get the peaks in decibels, whereby the signal X_{fft} is the fast Fourier transformed signal X .

$$X_{dB} = 20 \cdot \log_{10} \cdot \left(\frac{X_{fft}}{\sqrt{2} p_0} \right) \quad (5.8)$$

X_{dB}	...	scaled FFT signal in dB
X_{fft}	...	FFT signal in Pa
p_0	...	reference sound pressure, 20 μ Pa

The Matlab function "p octave" was used for the one-third-octave band analysis. Here it is important that the input $X_{poc,in}$ is the signal X divided by a reference sound pressure of 20 μ Pa.

$$X_{poc,in} = \frac{X}{p_0} = \frac{X}{20 \mu Pa} \quad (5.9)$$

To obtain the one-third-octave bands of the output signal from poctave in dB, the logarithm of the poctave's output $X_{\text{poc,out}}$ is multiplied by ten as follow:

$$X_{\text{dB,third}} = 10 \cdot \log_{10} \cdot (X_{\text{poc,out}}) \quad (5.10)$$

- $X_{\text{poc,in}}$ \cdots conditioned poctave's input signal
- $X_{\text{poc,out}}$ \cdots poctave's output signal
- $X_{\text{dB,third}}$ \cdots one-third-octave bands in dB

Taking the logarithm of all bands from $X_{\text{dB,third}}$, and multiplying the result by ten (addition of dB values), yields the total sound pressure level:

$$L_{\Sigma} = 10 \cdot \log_{10} \cdot \left(10^{\frac{L_1}{10}} + 10^{\frac{L_2}{10}} + \cdots + 10^{\frac{L_n}{10}}\right) \quad (5.11)$$

- L_{Σ} \cdots total sound pressure level in dB
- L_n \cdots sound pressure levels of the individual one-third-octave bands in dB

For illustration, Figure 5.11 shows step by step what the function "poctave" outputs and how the data is processed.

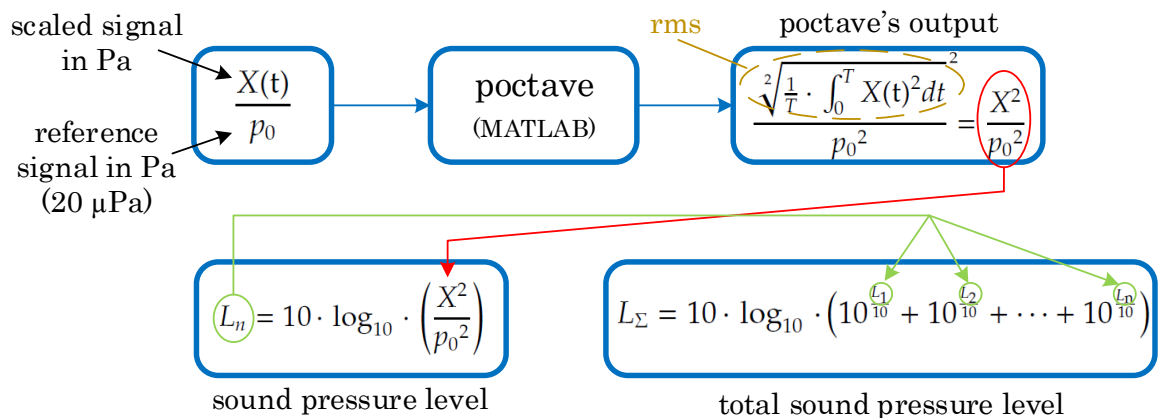


Figure 5.11: Stepwise illustration of "poctaves" output and the data processing for the microphones measurements.

Reciprocal distance law

It is often helpful to estimate the change in sound pressure level (SPL) in dB when the distance changes. Basically, every distance doubling causes a reduction of the SPL by 6 dB. Figure 5.12 shows a noise source and two different microphone positions at radii r_1 and r_2 recording the sound pressure levels L_1 and L_2 . The SPL change for point noise sources in the direct field (i.e., without air attenuation and frequency dependence), ΔL can be calculated as follow [51]:

$$\Delta L = L_2 - L_1 \quad (5.12)$$

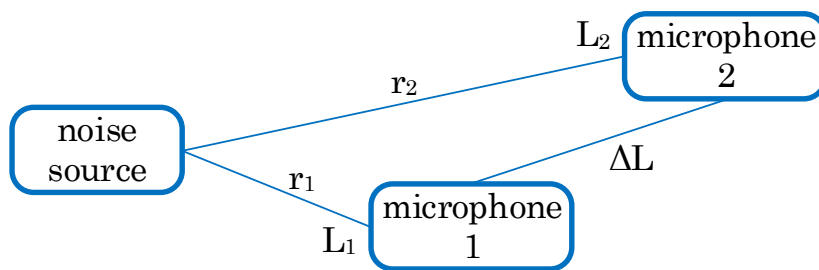


Figure 5.12: Change in SPL due to different microphone positions.

In general, the sound pressure level decreases by $1/r$ when increasing the distance to the sound source, which is called the reciprocal distance law. Equation (5.13) can be used to calculate L_2 in dB at radius r_2 in the direct field, knowing L_1 at radius r_1 [51].

$$L_2 = L_1 - \left| 20 \cdot \log_{10} \cdot \left(\frac{r_1}{r_2} \right) \right| = L_1 - \Delta L \quad (5.13)$$

- r_1 ... distance from the noise source to microphone 1 in m
- r_2 ... distance from the noise source to microphone 2 in m
- L_1 ... SPL of microphone 1 at r_1 in dB
- L_2 ... SPL of microphone 2 at r_2 in dB
- ΔL ... SPL change in dB

To validate the reciprocal distance law, two measurements, which are described in Chapter 5.6, are compared with the calculated values. The measurements were taken at a distance of 0.5 m in the near field and 1.0 m in the far field. The calculated sound pressure levels using (5.13) are contrasted with the measured ones in in Table 5.4.

Fansystem	position	near-field (0.5 m)	far-field (1.0 m)	calculated far-field (1.0 m)
E	LL	51.8 dB	46.2 dB	45.8 dB
L	LL	47.99 dB	41.93 dB	41.97 dB

Table 5.4: Comparison of the measured and calculated far-field SPLs. (The fan systems are listed in Table 5.3.)

Table 5.4 shows the measured SPLs of Fansystems E and L at distances of 0.5 m and 1 m as well as the calculated SPL at a distance of 1 m using the measured near-field values and (5.13). The measured and calculated far-field results are in excellent agreement, illustrating the usefulness of (5.13).

5.6 Measurement results

To validate the measurements as well as the data processing and signal conditioning, a separate SPL measuring device (Norsonic Nor140) was placed next to a microphone (position LL at a distance of 1 m) for comparison. Table 5.5 presents an excerpt of the performed measurements, comparing them to the results of the reference measuring device.

Fansystem	position	NTI M2230 (1.0 m)	Norsonic (1.0 m)
E	LL	46.25 dB(A)	45.65 dB(A)
J	LL	43.00 dB(A)	42.25 dB(A)
K	LL	42.50 dB(A)	41.85 dB(A)
L	LL	41.95 dB(A)	41.3 dB(A)

Table 5.5: Comparability of the measurement equipment. (The used fan systems are listed in Table 5.3.)

Since the values in Table 5.5 are very similar, it can be assumed performed measurements and evaluation thereof are correct.

5.6.1 Noise position dependence

It can be assumed that the sound pressure level of a radial fan system is position-dependent, given the inflow and outflow of air as well as the special shape of the housing. Figure 5.3 shows the different measuring positions of the near field measurements. It is expected that the inflow noise is dominant at position “LL”, the outflow noise is dominant at position “C”, and position “RR” is dominated by the switching and bearing noise. Figure 5.13 shows the sound power levels at the different measuring positions at a distance of 0.3 m.

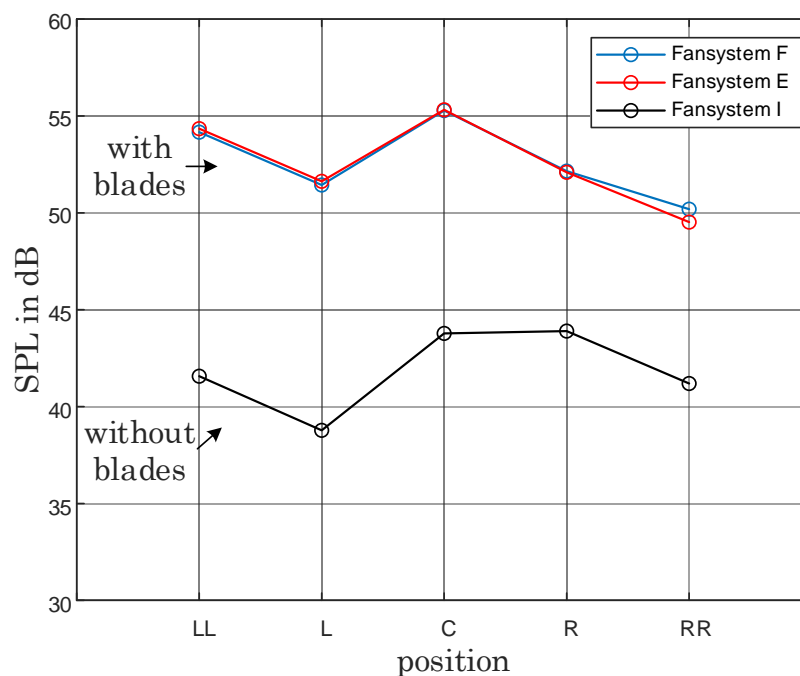


Figure 5.13: Measured SPLs of different fan systems at different positions.

Fansystems E and F show very similar results except for position “RR” in which Fansystem F is slightly louder than Fansystem E. The switching noise is assumed to be dominating at this position. It is clearly visible that the fan system without blades, Fansystem I, has a much lower sound pressure level than the others, which can be explained by the absence of aerodynamic noise. The variations in SPLs can be traced back to the different vibratory surfaces of the fan system.

5.6.2 Noise speed dependence

As discussed in Chapter 3.1, the noise of a fan system increases with increasing rotational speed. The sound pressure level as a function of the speed can be estimated with the help of an acoustic model law, e.g., according to Madison [43, p. 97 - 98]:

$$\Delta L = 10 \cdot \alpha \cdot \log_{10} \left(\frac{n_2}{n_1} \right) \quad (5.14)$$

- ΔL ... sound pressure level change in dB
- n_1 ... initial speed in rpm
- n_2 ... changed speed in rpm
- α ... average experience value [$4 \leq \alpha \leq 6$]

In order to measure this change Fansystems F-H are investigated, which differ in terms of operating speed (AMSS is the used control strategy). As shown in Figure 5.14, the SPL values were compared for different positions at a distance of 0.3 m.

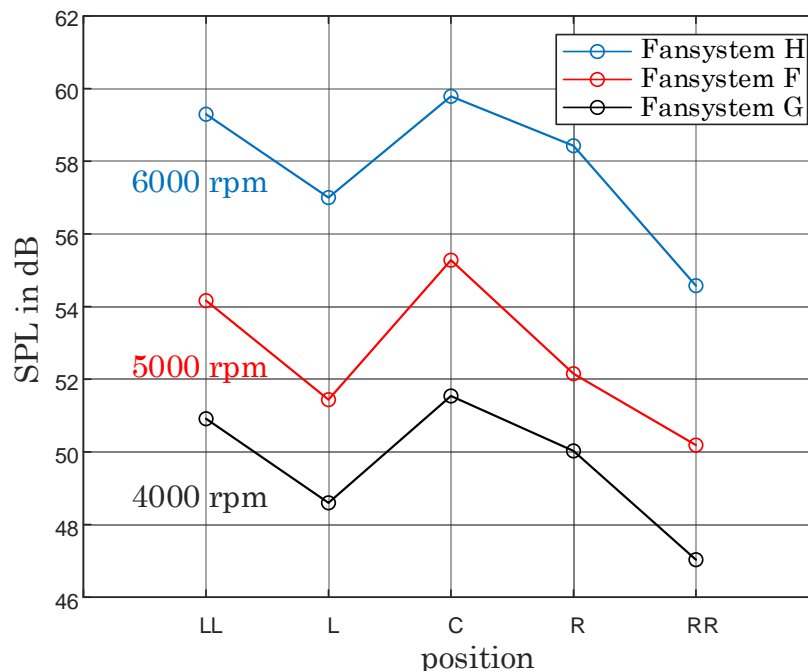


Figure 5.14: Measured SPLs of Fansystems F - H at different positions

All measuring points show the behavior described in (5.14) with the exception of measuring point “R” of Fansystem F. This could either be due to a measurement error or this speed does not excite the natural frequency of the housing in this direction. Since the presented measurement results are the average of three consecutive measurements in which the same behavior was observed, the second explanation is more likely.

Table 5.6 compares the 4000 rpm fan system (Fansystem F) as shown in Figure 5.14 with the calculated and measured values of the 6000 rpm fan system (Fansystem G) which has the same design.

Fansystem Table 5.3	position	measured SPL at 4000 rpm	measured SPL at 6000 rpm	calculated SPL from 4000 to 6000 rpm
G, H	LL	50.91 dB	59.30 dB	59.71 dB
G, H	L	48.60 dB	57.00 dB	57.40 dB
G, H	C	51.54 dB	59.79 dB	60.30 dB
G, H	R	50.03 dB	58.43 dB	58.83 dB
G, H	RR	47.03 dB	54.58 dB	55.80 dB

Table 5.6: Comparison of the measured and calculated SPL values, which are based on 4000 rpm. (The average experience value α is assumed to be 5.)

Table 5.6 shows that a good estimation of the increased SPL due to increased speed (and vice versa) can be made using (5.14). Furthermore, the Madison formula can also be used to estimate the sound pressure level for different fan diameters [43, p. 97 - 98]. Therefore (5.14) is extended as follows:

$$\Delta L = 10 \cdot \alpha \cdot \log_{10} \left(\frac{n_2}{n_1} \right) + 10 \cdot (\alpha + 2) \cdot \log_{10} \left(\frac{D_{o2}}{D_{o1}} \right) \quad (5.15)$$

- ΔL ... sound pressure level change in dB
- n_1 ... initial speed in rpm
- n_2 ... changed speed in rpm
- D_{o1} ... initial outer fan wheel diameter in m
- D_{o2} ... changed outer fan wheel diameter in m
- α ... average experience value [$4 \leq \alpha \leq 6$]

5.6.3 Separation of in- and outflow noise

As discussed in Chapter 3.4 and illustrated in Figure 3.4, turbulent in- and outflow noise is a characteristic property of radial fans. The literature describes that the turbulent inflow noise is in the lower and the turbulent outflow noise is in the upper frequency range with a possible overlap. To separate the in- and out flow noise, measurements were carried out as described in Chapter 5.1.2. It has been shown that measuring points 1 and 4 (see Figure 5.4 (b)) are good choices for evaluation, as they are sufficiently separated from each other. It is expected that the microphone at measuring point 1 measures primarily the turbulent inflow noise while the microphone at measuring point 4 measures essentially the turbulent outflow noise. Frequency ranges can be determined by comparing these measurements. Figure 5.15 shows order analyses for Fansystem E in Table 5.3.

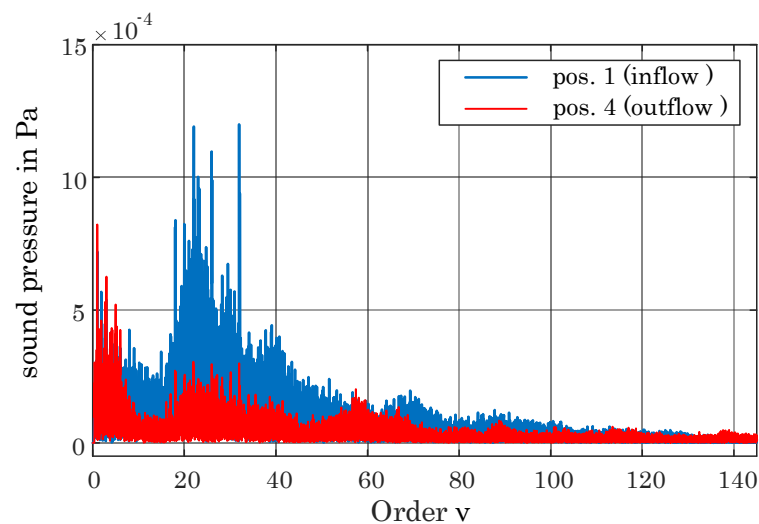


Figure 5.15: Order analyses of Fansystem E for microphone 1 in blue and microphone 4 in red.

The red outflow noise curve in Figure 5.15, which was measured at position 4, shows a clear attenuation of the amplitudes in the range of order 10 to 50, corresponding to a frequency range of 833 to 4166 Hz. This experiment was carried out for Fansystems E - H in Table 5.3 which differ in terms of control strategies and speeds but have the same housing. The frequency components in this range had the same behavior for all fan types. Therefore it was concluded that the turbulent inflow noise of the studied fan design is between 833 and 4166 Hz. According to the results, the turbulent outflow noise appears to be broadband over the whole frequency range.

5.6.4 Standardized measurements

The measurement of the **air-borne sound** has been carried out as discussed in Chapter 5.3. The industrial standard (VW 82469) was selected for the standardized measurements. Depending on the specific area of application, the one-third-octave band analysis of the fan system must comply with different limit curves as follow [50]:

- curve 1 passenger-operated auxiliary device which is activated when the combustion engine is switched on.
- curve 2 passenger-operated auxiliary device which is activated when the combustion engine is switched off and those which operate automatically when the combustion engine is switched on.
- curve 3 automatic auxiliary device when the combustion engine is switched off

For electrically powered vehicles the limit curve 3 must always be used. Furthermore, as described in Chapter 5.3, additional limit values of the total sound power level apply, which can be determined with (5.11) given the one-third-octave bands. The maximum total SPLs are specified as follows [50]:

- curve 1 with 65 db(A)
- curve 2 with 60 db(A)
- curve 3 with 55 db(A)

These limit values result, on the one hand, from the subjective perception of noise (see the actuating and disturbing noise discussed in Chapter 1.5). On the other hand, the audible and non-audible range discussed in Chapter 1.1 plays an important role.

It has been shown that the “inflow direction” is the loudest (see Figure 5.7), which is why it is evaluated in the following. Figure 5.16 shows the A-weighted 1/3 octave-band analysis of Fansystem E and Figure 5.17 shows that of Fansystem F, both measured at a distance of 0.5 m. Equation (5.11) results in a total sound power level of 51.81 dB(A) for Fansystem E and 52.10 dB(A) for Fansystem F. As can be seen, the one-third-octave-bands of Fansystems E and F at 1100 Hz already reach the limit curve 3.

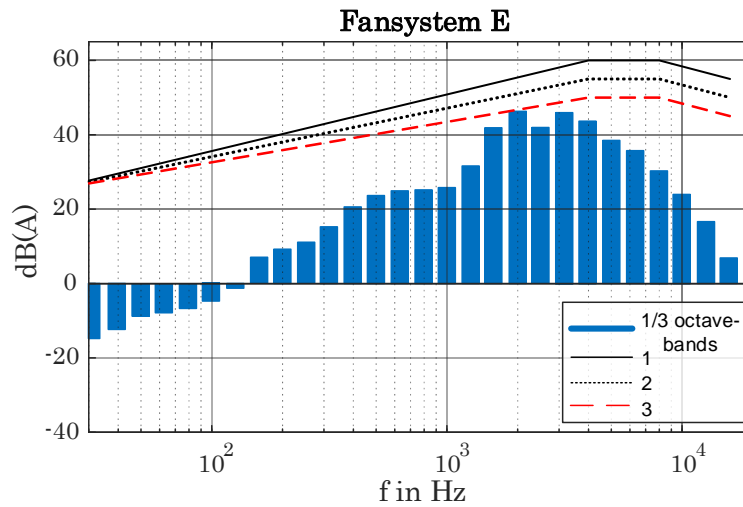


Figure 5.16: One-third-octave band analysis of the air-borne sound of Fansystem E and the limit curves.

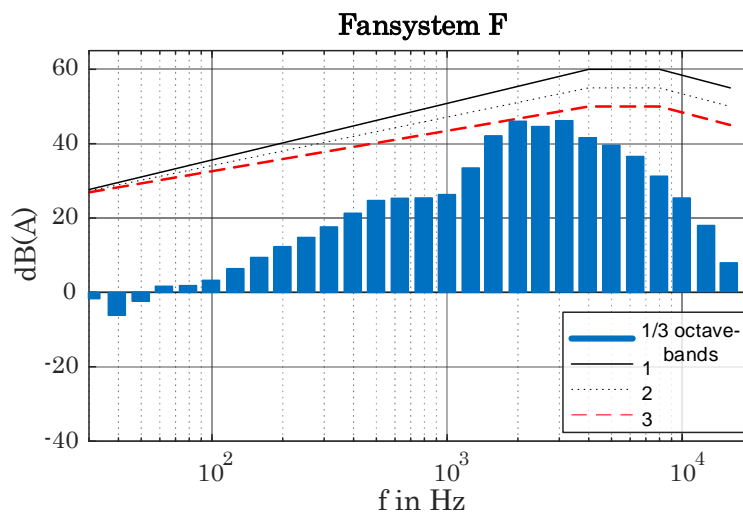


Figure 5.17: One-third-octave band analysis of the air-borne sound of Fansystem F and the limit curves.

The measurements of the **structure-borne sound** using acceleration sensors have been performed as described in Chapter 5.2.1 and the evaluation was carried out according to Chapter 5.5.1. Figure 5.18 shows the one-third-octave band analysis for Fansystem E and Figure 5.19 shows that of Fansystem F from Table 5.3. In Figures 5.18 and 5.19, the one-third-octave force spectrums of the x -, y -, and z -axis were added as described in Equation (5.5).

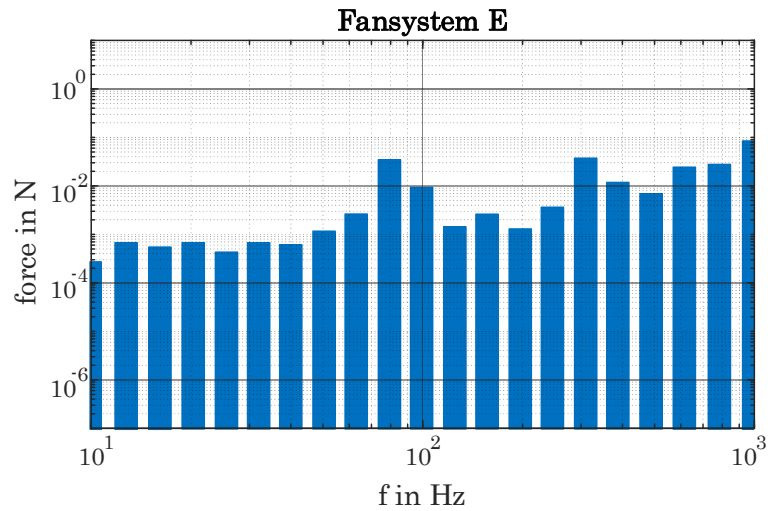


Figure 5.18: One-third-octave band analysis of the structure-borne sound of Fansystem E using acc. sensor and limit curves.

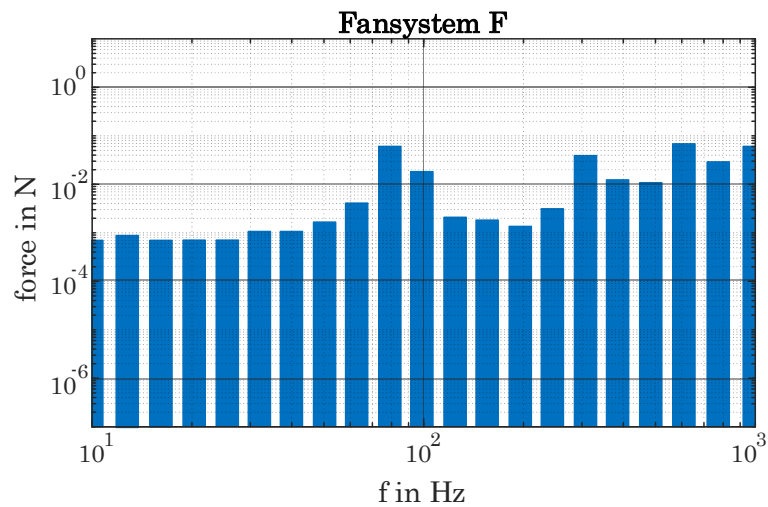


Figure 5.19: One-third-octave band analysis of the structure-borne sound of Fansystem F using acceleration sensor and limit curves.

The measurements of the **structure-borne sound** using force sensors (see Chapter 5.2.2) have been carried out as described in Chapter 5.3. The industry standard (VW 82469) was selected for the standardized measurements. Similar to the air-borne sound measurements, the standard provides application-dependent limit curves the product must not exceed. As characterized in the standard [50], all forces from all

attachment points are added (see 5.5) and represented as a one-third-octave band. As can be seen, while Fansystem M exceeds the limit curve 3, Fansystem N remains below the limits in the whole range.

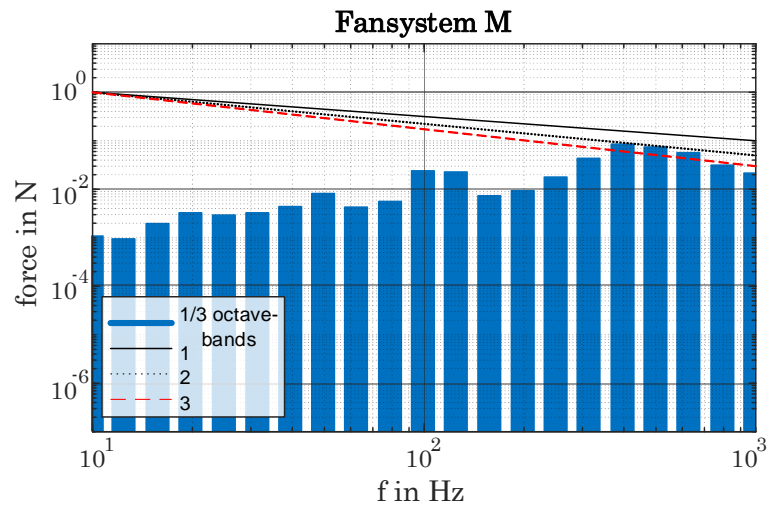


Figure 5.20: One-third-octave band analysis of the force measurement of Fansystem M and limit curves.

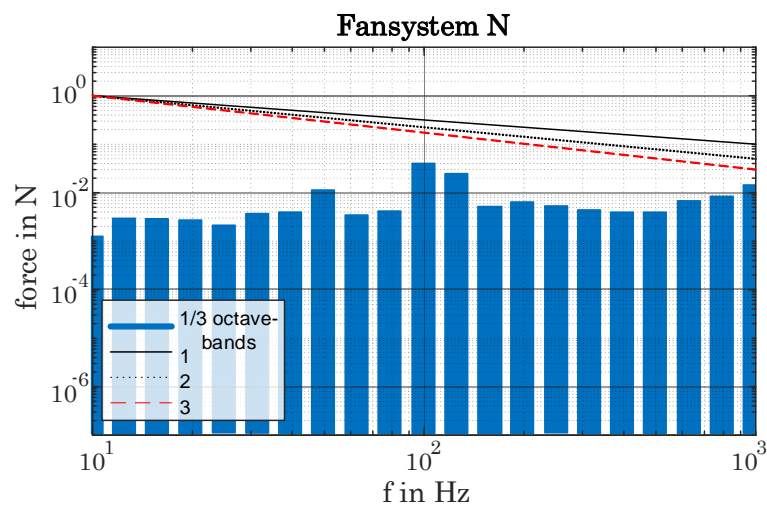


Figure 5.21: One-third-octave band analysis of the force measurement of Fansystem N and limit curves.

Chapter 6

Conclusions and future work

This Chapter concludes the findings of this thesis. In addition, an outlook for future work is given, which clearly goes beyond to scope of this thesis.

6.1 Conclusions

The demand for low-noise auxiliary drives in the automotive industry has increased as of late, because cars are becoming more and more quiet. This thesis studies the *Noise, Vibration, and Harshness* (NVH) characteristic of automotive auxiliary drives, especially those of fan systems. The aim is to identify the different noise sources and the occurring frequencies. As the first step, a literature review has been performed dealing with the state-of-the-art, the number and types of auxiliary drives in the automotive sector have been researched, and possible measuring methods to characterize the NVH behavior of these drives have been determined. A discussion of the function and the design of typical fan types as well as their aerodynamic and acoustic properties has been provided, with a particular focus on radial fans. The air-borne sound has been measured and evaluated with the use of microphones, while acceleration and force sensors have been used to determine the structure-borne sound. The supply current has been studied as well. It has been shown that by removing the fan blades a significantly reduction of the aerodynamic noise can be reached to simplify the allocation of mechanically and electromagnetically generated noise components. It has also been shown that the separation of the turbulent in- and outflow noise of radial fan systems is difficult due to small dimensions and close proximity of the in- and outlet. In addition, the occurring frequencies as well as the sound pressure level (SPL) strongly depend on the measuring position, the rotating speed, and the mechanical transfer function of the housing. However, an

analytical approximation of the SPL changes for changing speed and distance has been evaluated experimentally resulting in excellent agreement. A typical characteristic of axial fan is the blade passing noise (BPN), which dominates their total sound spectrum. The tested radial fan drives also showed this characteristic, but in an attenuated form. The main part of aerodynamic noise showed the expected broadband noise due to air turbulences in addition to interference noise due to the natural frequency of the housing. Especially significant in the noise and vibration spectrum is an imbalance of the rotor, which can be caused by manufacturing tolerances or defects. This makes it particularly important to minimize imbalances beforehand as much as possible. In contrast, it has been found that magnetostriction and coil deformation play a minor role in the overall development of auxiliary drives. This can be explained by the relatively large air-gap, small iron core dimensions, and usage of non-grain-oriented electrical steel sheets. For these single phase applications, it has been shown that measuring of the supply current is sufficient to determine the excitation frequencies of the electromagnetic noise. (A measurement of the coil-currents is therefore not necessary.) Furthermore, having knowledge of the approximate current shape, the occurring frequencies can be obtained from a discrete Fourier-transformation of a piecewise linear approximation of the current. On the one hand the measurements and evaluations, carried out according to the selected industrial standard, have posed a great challenge. On the other hand, it has been shown how important the correct scaling and processing of measurement data is.

6.2 Future work

The results of this thesis provide a useful foundation for future research. Some suggestions are described below.

- An important next step would be to perform a modal analysis of the fan housing to determine the natural frequencies.
- A laser vibrometer may be used for precise non-contact measurements in which the mass of the sensors does not influence the results. However, the surface (and color) of the device under test may influence the quality of the measurements.

- Furthermore, the implementation of a very high resolution microphone array measurement may be helpful to achieve a more precise localization of the noise.
- Acoustic measurements of the fan system should be performed when it is installed in the application, as the mechanical structure changes and potentially also the emitted noise.
- Experiments at lower speeds may be performed to investigate the influence of the cogging torque on the noise spectrum. All tests carried out in this thesis have a speed at which the aerodynamic noise components dominate the spectrum.

Bibliography

- [1] P. Zeller, *Handbuch Fahrzeugakustik - Grundlagen, Auslegung, Berechnung, Versuch*. Berlin Heidelberg New York: Springer-Verlag, 2009.
- [2] S. Leitner, H. Gruebler, and A. Muetze, "Cogging torque minimization and performance of the sub-fractional hp bldc claw-pole motor," *IEEE Transactions on Industry Applications*, vol. 55, no. 5, pp. 4653–4664, Sep. 2019.
- [3] Zentralverband Elektrotechnik- und Elektronikindustrie e. V. (ZVEI), "Elektrische Antriebe - Wirtschaftliche Entwicklung 2010 bis 2018," Jan. 2019.
- [4] R. Fischer, *Elektrische Maschinen*, 17th ed. München: Hanser Verlag, 2017.
- [5] W. Hofmann, *Elektrische Maschinen - Lehr- und Übungsbuch*. München: Pearson, 2013.
- [6] H. D. Stölting, E. Kallenbach, and W. Amrhein, *Handbuch elektrischer Kleinantriebe*, 4th ed. München: Hanser Verlag, 2011.
- [7] H. Tschoeke, *Die Elektrifizierung des Antriebsstrangs - Basiswissen*. Wiesbaden, Deutschland: Springer Verlag, 2015.
- [8] C. Kinnaird, "How many electric motors are in your car?" Mar. 2018, [Accessed: Feb. 08, 2019]. [Online]. Available: https://e2e.ti.com/blogs_/b/behind_the_wheel/archive/2018/03/29/how-many-electric-motors-are-in-your-car#
- [9] J. Hagedorn, F. Sell-Le Blanc, and J. Fleischer, *Handbuch der Wickeltechnik für hocheffiziente Spulen und Motoren*. Berlin: Springer Verlag, 2016.
- [10] H. Hembach, "Systematischer Vergleich von BLDC-Motorkonzepten mit Anwendung auf nass laufende Wasserpumpen kleiner Leistung," Ph.D. dissertation, Bundeswehr Universität München, Neubiberg, 28.11.2007.

- [11] P. Upadhayay, "Mit über 100 kleinen Stellmotoren - Die neue S-Klasse," Jul. 2013, [Accessed: Feb. 08, 2019]. [Online]. Available: <https://blog.mercedes-benz-passion.com/2013/07/mit-uber-100-kleinen-stellmotoren-die-neue-s-klasse/>
- [12] Nidec Corporation, "Nidec motors and actuators," [Accessed: Feb. 12, 2019]. [Online]. Available: <http://nidec-ma.de/en/productlist.html>
- [13] ebm-papst GmbH, [Accessed: Feb. 08, 2019]. [Online]. Available: https://www.ebmpapst.com/de/products/compact-fans/compact_fans.html
- [14] Pierburg pump technology, "Ölpumpen für Verbrennungsmotoren und getriebe," [Accessed: Feb. 14, 2019]. [Online]. Available: https://cdn.rheinmetall-automotive.com/fileadmin/media/kspg/Broschueren/Produktbroschueren/Pierburg_Pump_Technology/Oelpumpen/ppt_oelpump_verbrennung_d.pdf
- [15] Robert Bosch GmbH, "bosch-mobility-solutions," [Accessed: Feb. 14, 2019]. [Online]. Available: <https://www.bosch-mobility-solutions.de/de/produkte-und-services/pkw-und-leichte-nutzfahrzeuge/innenraum-und-karosseriesysteme/komfortantriebe/>
- [16] Johnson Electric, "Actuators (automotive)," [Accessed: Feb. 14, 2019]. [Online]. Available: <https://www.johnsonelectric.com/en/product-technology/motion/actuators-automotive>
- [17] J. Zhao and Y. Yu, "Brushless dc motor fundamentals application note," online, Jul. 2011, [Accessed: Jan. 22, 2019]. [Online]. Available: https://www.monolithicpower.com/pub/media/document/Brushless_DC_Motor_Fundamentals.pdf
- [18] Electrical Technology, "brushless dc motor, construction, working principle and applications," [Accessed: Jun. 19, 2019]. [Online]. Available: <https://www.electricaltechnology.org/2016/05/bldc-brushless-dc-motor-construction-working-principle.html>
- [19] D. Hanselman, *Brushless Permanent Magnet Motor Design*, 2nd ed. Ohio, USA: Magna Physics Publishing, 2006.

- [20] H. Gruebler, S. Leitner, A. Muetze, and G. Schoener, "Improved switching strategy for a single-phase brushless direct current fan drive and its impact on efficiency," *IEEE Transactions on Industry Applications*, vol. 54, no. 6, pp. 6050–6059, Nov 2018.
- [21] D. Collins, "what is the difference between BLDC and synchronous ac motors," Motion Control Tops, Dec. 2015, [Accessed: Jun. 11, 2019]. [Online]. Available: <https://www.motioncontroltips.com/faq-whats-the-difference-between-blcdc-and-synchronous-ac-motors/>
- [22] D. Wilson, "Motor control compendium," 2010, [Accessed: Jul. 1, 2019]. [Online]. Available: www.ti.com/download/trng/docs/c2000/TI_MotorControlCompendium_2010.pdf
- [23] C. Chiu, Y. Chen, Y. Liang, and R. Liang, "Optimal driving efficiency design for the single-phase brushless dc fan motor," *IEEE Transactions on Magnetics*, vol. 46, no. 4, pp. 1123–1130, April 2010.
- [24] Y. Chen, C. Chiu, Z. Tang, Y. Liang, and R. Liang, "Optimizing efficiency driver comprising phase-locked loop for the single-phase brushless dc fan motor," *IEEE Transactions on Magnetics*, vol. 48, no. 5, pp. 1937–1942, May 2012.
- [25] F. Krall, H. Gruebler, and A. Mütze, "Angle Modulated Switching Strategy for Fractional Horsepower BLDC Motors for Improved Electromagnetic Compatibility," in *2019 21th European Conference on Power Electronics and Applications (EPE'19 ECCE Europe)*, Sep. 2019, pp. P.1–P.7.
- [26] S. Dunkl, "Control aspects of single and three phase pm drives in fraction power applicatins," Ph.D. dissertation, Graz University of Technology, Jan. 2016.
- [27] J. F. Gieras, C. Wang, and J. C. Lai, *Noise of Polyphase Electric Motors*. 6000 Broken Sound Parkway NW, Suite 300 Boca Raton, FL 33487-2742: Taylor & Francis Group, LLC, 2006.
- [28] H. Moczala, *Elektrische Kleinmotoren, Wirkungsweise, Bauformen, Eigenschaften - Hinweise für den Einsatz.*, 2nd ed. Ehningen bei Böblingen: Expert Verlag, 1993.
- [29] "Acoustics determination of airborne sound power levels emitted by machinery using vibration measurement," ÖNORM, ISO \ TS 7849, Oct. 2017.

- [30] Kistler GmbH, “Ceramic shear ultraminiatur-beschleunigungssensor tropfenform, 500g,” [Accessed: Mar. 06, 2019]. [Online]. Available: <https://www.kistler.com/de/produkt/type-8778a500/>
- [31] ebm-papst GmbH, “Technology-basic principles,” Apr. 2015, [Accessed: Jun. 13, 2019]. [Online]. Available: https://www.google.com/search?client=firefox-b-d&q=ebm_papst_Technology_basic_principle_EN#
- [32] R. Haermeyer, A. Lelkes, and J. Adam, “Kühlung elektronischer systeme (tutorial),” 11 2004.
- [33] K. Azar, “How to effectively use fan trays in electronic systems,” Aug. 2009, [Accessed: Jun. 17, 2019]. [Online]. Available: https://www.eetimes.com/document.asp?doc_id=1272153#
- [34] A. Farschtschi, *Elektromaschinen in Theorie und Praxis*, 1st ed. Berlin: VDE Verlag, 2001.
- [35] K. Knut, “Vibrationen und Geräusche von elektrischen Antrieben.” Essen: Haus der Technik, 2017, [seminar].
- [36] P. L. Timár, A. Fazekas, J. Kiss, A. Miklós, and S. J. Yang, *Noise and Vibration of Electrical Machines*. Amsterdam-Oxford-New York-Tokyo: Elsevier, 1989.
- [37] R. P. Lisner and P. L. Timar, “A new approach to electric motor acoustic noise standards and test procedures,” *IEEE Transactions on Energy Conversion*, vol. 14, no. 3, pp. 692–697, Sep. 1999.
- [38] K. Xia, J. Lu, B. Dong, and C. Bi, “Analysis of acoustic noise from electromagnetic torque ripple for brushless dc motor,” in *2016 Asia-Pacific Magnetic Recording Conference Digest (APMRC)*, July 2016, pp. 1–2.
- [39] S. Subramaniam, A. Petr, and M. O. I. Ing, “Unified noise characterization technique for mosfets,” in *2017 International Conference on Noise and Fluctuations (ICNF)*, June 2017, pp. 1–5.
- [40] H. Janocha, *Aktoren, Grundlagen und Anwendung*, 1st ed. Springer-Verlag, 1992.
- [41] J. Bacher, “Elektrische Maschinen für die Energietechnik,” 2015, IV 431.257.

- [42] F. Schwenker, "Aspects of high performance flat external rotor motors," in *Innovative Small Drives and Micro-Motor Systems; 12. ETG/GMM Symposium*, Sep. 2019, pp. 152–155.
- [43] T. Carolus, *Ventilatoren, Aerodynamischer Entwurf, Schallvorhersage, Konstruktion*, 3rd ed. Siegen, Deutschland: Springer Verlag, 2013.
- [44] European Patent Office, "Radialventilatoren und Düse für einen Radialventilator," Germany European Patent EP 1 122 444 A2, Aug. 8, 2001.
- [45] M. Thomsen, "Online Condition Monitoring von Windenergieanlagen mittels Körperschallanalyse," Master's thesis, Fachhochschule Flensburg, Gesellschaft für Energie und Ökologie, Jul. 2002.
- [46] J. Le Besnerais, Q. Souron, and E. Devillers, "Analysis of the electromagnetic acoustic noise and vibrations of a high-speed brushless dc motor," in *8th IET International Conference on Power Electronics, Machines and Drives (PEMD 2016)*, April 2016, pp. 1–10.
- [47] GfM Gesellschaft für Maschinendiagnose mbH, "Kompendium - Wälzlagerkinematik," [Accessed: Feb. 13, 2019]. [Online]. Available: <https://maschinendiagnose.de/kompendium-waelzlagerkinematik.html>
- [48] *Industrial fans - Determination of fan sound power levels under standardized laboratory conditions - Part 3*, International Standard ISO 13347-3, 2004.
- [49] *Geräuschmessung an Maschinen, Luftschallemission, Hüllflächen-, Hallraum-, und Kanal- Verfahren - Ventilatoren*, Deutsche Norm DIN 45 635 Teil 38, 1986.
- [50] Dr. Friedrich Bielert, *Zusatzaggregate - Akustische Anforderungen*, Volkswagen Konzernnorm VW 82 469, Jul. 2014.
- [51] "Tontechnik-Rechner - sengpielaudio," [Accessed: .Aug. 30, 2019]. [Online]. Available: <http://www.sengpielaudio.com/Rechner-entfernung.htm>

List of figures

1.1	Schematic in-car noise development [1, p. 394].	1
1.2	Percentage distribution of the production volume of electric drives in 2017 [3, p. 3].	2
1.3	Overview of the usage of small electric drives in a car [9, p. 81].	4
1.4	Percentage distribution of small electric drives in a mid-size executive car [10, p. 7].	5
1.5	Equivalent circuit of a single-phase BLDC motor [20].	9
1.6	Idealized current and back-EMF waveforms of a BLAC (a) and a BLDC (b) motor [19, p. 186].	10
1.7	Generic current waveform for square wave commutation indicating the switching [23, p. 1123 - 1127], [24, 1937 - 1939].	11
1.8	Simplified comparison of the construction between a single-phase (a) and a three-phase (b) stator [17, p. 7].	12
1.9	Schematic circuit of a single-phase BLDC motor with (a) unifilar [26, p. 21] and (b) bifilar winding [20, p. 3]	13
1.10	Possible control techniques of a single-phase BLDC motor [26, p. 65].	13
1.11	Inverter circuit of a single-phase BLDC motor: (a) full bridge for unifilar and (b) two-switch inverter for bifilar winding [26, p. 66 - 71].	14
1.12	Subjective human sound perception as a function of frequency [27, p. 3].	16
1.13	Artificial head.	18
1.14	Flow of noise assessment process [6, p. 381].	19
2.1	Different fan types with the airflow direction [31, p. 6].	22
2.2	Aerodynamic relationship between the volume rate and the air pressure of the different fan types of the same size and speed [32, p. 4].	23
2.3	Typical fan curves and their optimal operating range [31, p. 7].	24
2.4	Determination of the fan's operating point [32, p. 9].	24

2.5	Rotor of an axial fan with seven blades.	25
2.6	Radial fan with forward-curved blades and scroll housing.	26
3.1	Sources of noise and vibration [35, p. 54].	30
3.2	Typical composition of the noise sources depending on the rotational speed for constant output power [37, p. 693].	30
3.3	Electromagnetic sources [38].	33
3.4	Generic noise spectrum of a fan [1, p. 398].	35
3.5	Basic acoustic and aerodynamic correlations [31, p. 106 - 108].	37
3.6	Geometry and definition of the used variables [45, p. 9].	38
3.7	Magnetic sound development [34, p. 490].	41
4.1	Microphone measuring setup (a) and positions (b).	44
4.2	Acceleration and current measuring setup.	45
4.3	Typical radial fan rotor and modified rotor.	47
4.4	Schematic experimental setup for the stator excitation investigations.	48
4.5	Measured coil currents in (a) and supply and added coil currents in (b) of the Fansystem E. The order analyses are illustrated on the right.	50
4.6	Measured supply current and its order analysis of the Fansystem F operated with AMSS.	51
4.7	Measured current of Fansystem I and its order analysis.	51
4.8	Comparison of the measured currents and order analysis of Fansystems E and I.	52
4.9	Comparison of simulated and measured currents of Fansystem E.	52
4.10	Comparison of simulated and measured currents of Fansystem F.	53
4.11	Comparison of simulated and measured currents of Fansystem I.	53
4.12	Positions of additional masses for imbalance investigations.	54
4.13	Change in the first order compared of Fansystem A for different imbalances measured with an acceleration sensor.	55
4.14	Example of blade passing noise of Fansystem C	56
4.15	Comparison of the occurring frequencies of the supply current, acceleration sensor, and microphone of position 6 (see Figure 4.1 (b)) measurements.	57
4.16	Comparison of the occurring frequencies of the microphone measurement at position 2 (see Figure 4.1 (b)) of three different fan systems from Table 4.3.	58

5.1	Overview of the performed measurements.	59
5.2	Test setup for the near and far-field measurements using microphone arrays.	61
5.3	Closeup showing the near-field measurement setup (a) and microphone positions for the near- and far-field array measurements (b).	61
5.4	Measurement setup (a) and the positions of the microphones (b).	62
5.5	Measurement setup for the acceleration measurements.	63
5.6	Measurement setup for the force measurements.	64
5.7	Measurement setup for the standardized measurement.	65
5.8	Block diagram for scaling of the accelerometer signal.	67
5.9	Stepwise illustration of “poctaves” output and the data processing for the force measurements.	69
5.10	Block diagram for scaling of the microphone signal.	69
5.11	Stepwise illustration of “poctaves” output and the data processing for the microphones measurements.	71
5.12	Change in SPL due to different microphone positions.	72
5.13	Measured SPLs of different fan systems at different positions.	74
5.14	Measured SPLs of Fansystems F - H at different positions	75
5.15	Order analyses of Fansystem E for microphone 1 in blue and microphone 4 in red.	77
5.16	One-third-octave band analysis of the air-borne sound of Fansystem E and the limit curves.	79
5.17	One-third-octave band analysis of the air-borne sound of Fansystem F and the limit curves.	79
5.18	One-third-octave band analysis of the structure-borne sound of Fansystem E using acc. sensor and limit curves.	80
5.19	One-third-octave band analysis of the structure-borne sound of Fansystem F using acceleration sensor and limit curves.	80
5.20	One-third-octave band analysis of the force measurement of Fansystem M and limit curves.	81
5.21	One-third-octave band analysis of the force measurement of Fansystem N and limit curves.	81

List of tables

1.1	Number of auxiliary drives to increase the comfort of the Mercedes S-Class in 2013 [11].	5
1.2	Automotive applications and their motor types [12–16].	7
3.1	Typical causes of noise and vibration [36, p. 269].	42
4.1	Used components of the measurement.	44
4.2	Used components for the acceleration and current measurements. . .	46
4.3	Fan systems under investigation.	46
5.1	Used components for the air-borne sound measurements.	60
5.2	Used components for the structure-borne sound measurement.	63
5.3	Fan systems under investigation.	66
5.4	Comparison of the measured and calculated far-field SPLs. (The fan systems are listed in Table 5.3.)	73
5.5	Comparability of the measurement equipment. (The used fan systems are listed in Table 5.3.)	73
5.6	Comparison of the measured and calculated SPL values, which are based on 4000 rpm. (The average experience value α is assumed to be 5.)	76